MITIGATION OF LIGHT INDUCED DEGRADATION AND, LIGHT AND ELEVATED TEMPERATURE INDUCED DEGRADATION MECHANISMS IN BORON DOPED CZOCHRALSKI GROWN SILICON WAFERS

A THESIS SUBMITTED TO
THE GRADUATE SCHOOL OF NATURAL AND APPLIED SCIENCES
OF
MIDDLE EAST TECHNICAL UNIVERSITY

BY

VAHDET ÖZYAHNİ

IN PARTIAL FULFILLMENT OF THE REQUIREMENTS
FOR
THE DEGREE OF MASTER OF SCIENCE
IN
MICRO AND NANOTECHNOLOGY

JANUARY 2024

Approval of the thesis:

THESIS TITLE

submitted by **VAHDET ÖZYAHNİ** in partial fulfillment of the requirements for the degree of **Master of Science in Micro and Nanotechnology, Middle East Technical University** by,

Prof. Dr. Halil Kalıpçılar
Dean, Graduate School of **Natural and Applied Sciences** ________________

Prof. Dr. Deniz Üner
Head of the Department, **Micro and Nanotechnology** ________________

Prof. Dr. Raşit Turan
Supervisor, **Micro and Nanotechnology, METU** ________________

Assoc. Prof. Dr. Selçuk Yerci
Co-Supervisor, **Electrical and Electronics Eng., METU** ________________

Examining Committee Members:

Prof. Dr. Hüsnü Emrah Ünalan
Metallurgical and Materials Eng, METU ________________

Prof. Dr. Raşit Turan
Physics, METU ________________

Assoc. Prof. Dr. Hande Toffoli
Physics, METU ________________

Prof. Dr. Alpan Bek
Physics, METU ________________

Assist. Prof. Dr. Veysel Ünsür
Basic Sciences, Necmettin Erbakan University ________________

Date: 08.01.2024

I hereby declare that all information in this document has been obtained and presented in accordance with academic rules and ethical conduct. I also declare that, as required by these rules and conduct, I have fully cited and referenced all material and results that are not original to this work.

Name Last name : Vahdet Özyahni

Signature :

ABSTRACT

MITIGATION OF LIGHT-INDUCED DEGRADATION AND, LIGHT AND ELEVATED TEMPERATURE INDUCED DEGRADATION MECHANISMS IN BORON DOPED CZOCHRALSKI GROWN SILICON WAFERS

Özyahni, Vahdet
Master of Science, Micro and Nanotechnology
Supervisor: Prof. Dr. Raşit Turan
Co-Supervisor: Assoc. Prof. Dr. Selçuk Yerci

January 2024, 74 pages

The degradation of solar cells is critical for their long-term performance. If the recombination concentration is high, the rate of electricity generation from the solar cell will be lowered significantly.

Within this thesis, two commonly known degradation mechanisms of light-induced degradation (LID) and, light and elevated temperature-induced degradation (LeTID) on boron doped silicon wafers were investigated. To understand the effect of base resistivity on B-O LID defect mechanism, three different base resistivity groups of samples with 0.2, 1.5 and 650 Ω.cm were used as substrates. Also, a fast regeneration method that is an alternative to illuminated annealing with halogen lamp and hot plate method, was proposed by a 915 nm diode laser. Moreover, two different silicon nitride (SiN_x) passivation layers were deposited to identical samples to investigate the effect of different passivation layers on both LID and LeTID mechanisms.

According to the results, 0.2 and 1.5 Ω.cm base resistivity samples showed a significant degradation due to B-O defects, while 650 Ω.cm base resistivity samples did not at all. Moreover, the concentration of hydrogen that diffused from both SiN_x

passivation layers to bulk was calculated. Diffused hydrogen concentrations from both passivation layers were enough for the passivation of B-O defects in each base resistivity sample. Although there was a significant difference in the concentration of diffused hydrogen atoms inside the bulk, the extent of LeTID was identical for differently passivated SiN_x samples. However, it was seen that increased hydrogen concentration inside the bulk caused a faster formation of LeTID.

Keywords: LID, LeTID, hydrogen, silicon nitride, base resistivity

ÖZ

BOR KATKILANMIŞ CZOCHRALSKI METODUYLA BÜYÜTÜLMÜŞ KRİSTAL SİLİSYUM ÖRNEKLERDE IŞIKLA İNDÜKLENEN BOZUNMA VE IŞIK VE SICAKLIKLA İNDÜKLENMİŞ BOZUNMANIN AZALTILMASI

Özyahni, Vahdet
Yüksek Lisans, Mikro ve Nanoteknoloji
Tez Yöneticisi: Prof. Dr. Raşit Turan
Ortak Tez Yöneticisi: Doç. Dr. Selçuk Yerci

Ocak 2024, 74 sayfa

Güneş hücrelerinde meydana gelen verim düşürücü kusurlar uzun vadeli performansları açısından kritik öneme sahiptir. Bu sebeple, fazla miktarda verim düşürücü kusur içeren güneş hücrelerinde yüksek miktarda elektrik üretiminde düşüş gözlemlenebilir.

Bu tezde, boron katkılanmış silisyum örnekler üzerinde ışıkla indüklenen bozunma (LID) ve ışık ve yüksek sıcaklıkla indüklenen bozunma (LeTID) araştırıldı. Kitle direncinin kusur sebepli bozunmaların üzerindeki etkilerini anlayabilmek için üç farklı kitle direncine sahip 0.2, 1.5 ve 650 Ω.cm örnek grubu kullanıldı. B-O kusurlarının pasivasyonuna hızlı ve etkin bir yöntem olarak 915 nm diyot lazer metodu halojen lamba ve sıcak plaka kullanılarak yapılan pasivasyona alternatif olarak sunuldu. Ayrıca, hidrojen konsantrasyonunun hem LID hem de LeTID mekanizmları üzerindeki etkisini araştırmak için iki farklı silisyum nitrür (SiN_x) pasivasyon katmanı denk örneklere ayrı olarak büyütüldü.

Sonuçlara göre, 0.2 ve 1.5 Ω.cm kitle direncine sahip örneklerde B-O kusurlarından dolayı önemli miktarda bir bozunma görülürken 650 Ω.cm kitle direncine sahip örneklerde hiç bir bozulma gözlemlenmedi. Her iki SiN_x pasivasyon katmanından tavlama işlemi sırasında kitle içerisine yayılan hidrojen konsantrasyonu hesaplandı. Her iki pasivasyon katmanından kitle içerisine yayılan hidrojen konsasntrasyonunda olmasına rağmen, farklı SiN_x katmanıyla pasifleştirilmiş örnekler için LeTID sebepli kusurlar kaynaklı düşüşün aynı miktarda olduğu gözlemlendi. Ancak kitle içerisinde artan hidrojen konsantrasyonun daha hızlı bir LeTID sebepli düşüşe neden olduğu saptandı.

Anahtar Kelimeler: LID, LeTID, hidrojen, silisyum nitrür, kitle direnci

To my family

ACKNOWLEDGMENTS

I wish to express my deepest gratitude to my supervisor Prof. Dr. Raşit Turan for his guidance, advice, criticism, encouragement, and insight throughout the research. He gave me a valuable opportunity to work in a high-standard facility with an exceptional team.

I would like to share my gratitude with my co-supervisor Assoc. Prof. Dr. Selçuk Yerci and committee members: Prof. Dr. Emrah Ünalan, Prof. Dr. Alpan Bek, Assoc. Prof. Dr. Hande Toffoli, and Assist. Prof. Dr. Veysel Ünsür.

I want to especially thank Dr. Gence Bektaş for his motivation, suggestions and valuable friendship. It is always enjoyable working with him. He showed me the importance of looking from an appropriate perspective both in science and life.

I want to thank my co-workers Hasan Hüseyin Canar, Sercan Aslan, Selin Seyrek, Ahmet Emin Keçeci, Gülçin Çelik and Hasan Asav for their friendship and help with my thesis. It was a pleasure to share time with them.

The technical assistance of Murat Aynacıoğlu, Batuhan Taş and Furkan Çiçek are gratefully acknowledged.

Last but not least, my family always encouraged and supported me whenever I need. Also, my dearest soul partner Ekin Galioğlu, never let me down and supported me without hesitation.

This work is funded by Scientific and Technological Research Council of Turkey under grant number TUBİTAK 20AG002.

TABLE OF CONTENTS

ABSTRACT v

ÖZ vii

ACKNOWLEDGMENTS x

TABLE OF CONTENTS xi

LIST OF TABLES xv

LIST OF FIGURES xvi

LIST OF ABBREVIATIONS xix

LIST OF SYMBOLS xx

1 INTRODUCTION 1

1.1 Czochralski Grown Silicon Wafers 2

1.2 Passivated Emitter and Rear Cell (PERC) 3

1.3 Solar Cell Parameters 4

1.3.1 Current vs Voltage Curve (I-V) 4

1.3.2 Open Circuit Voltage (V_{oc}) 5

1.3.3 Short Circuit Current (I_{sc}) 5

1.3.4 Fill Factor (FF) 6

1.3.5 Efficiency (η) 6

1.4 Recombination 7

1.4.1 Radiative Recombination 7

1.4.2 Auger Recombination 8

1.4.3 Shockley-Read-Hall Recombination 9
1.5 Defects in the Bulk 10
1.5.1 Intrinsic Defects 10
1.5.2 Extrinsic Defects 11
1.6 Motivation of Thesis 11
2 THEORY AND BACKGROUND 13
2.1 Light Induced Degradation (LID) 13
2.1.1 B-O Defects 15
2.1.2 Passivation of B-O Defects 16
2.1.3 The Effect of Base Resistivity on LID 19
2.1.4 Fe-B Pairs 19
2.1.5 Passivation of Fe-B Pairs 21
2.2 Light and Elevated Temperature Induced Degradation (LeTID) 22
2.3 Hydrogen Atoms Inside the Bulk 23
2.3.1 SiN_x:H Passivation Layer 24
2.3.2 Hydrogen Diffusion Mechanism 25
2.3.3 Base Resistivity Variation by B-H Bonds 26
3 EXPERIMENTAL 29
3.1 PERC Sample Fabrication 29
3.1.1 Characteristics of Wafers 30
3.1.2 Samples Surface Morphology Modifications 32
3.1.3 Emitter Formation 32
3.1.4 Al_2O_3 Deposition 33
3.1.5 SiN_x Deposition 33

3.1.6 Laser Contact Opening (LCO) 34
3.1.7 Screen Printing 34
3.1.8 Firing 34
3.2 Lifetime Sample Preparation 35
3.3 Investigation of LID and LeTID 36
3.3.1 LID Treatment 36
3.3.2 Calculation of [Fe_i] Inside the Bulk 37
3.3.3 Calculation of [H_{tot}] Inside the Bulk 37
3.3.4 LeTID Treatment 37
3.4 Characterization Methods 38
3.4.1 Sinton WCT120TS Lifetime Tester 38
3.4.2 Sinton SunsV_{oc} Tester 39
3.4.3 Sun I-V Sorter 39
4 RESULTS AND DISCUSSION 41
4.1 Fabricated Samples 41
4.2 Investigation of LID 44
4.2.1 Optimization of Degradation Process 44
4.2.2 Dark Annealing Enhanced Degradation Process 47
4.2.3 Optimization of Regeneration Process 49
4.2.4 Determination of Diffused Hydrogen Concentration Inside the Bulk 55
4.2.5 Calculation of Iron Impurities 58
4.3 Investigation of LeTID 59
5 CONCLUSION 61

REFERENCES 63

LIST OF TABLES

TABLES

Table 3.1: *Characteristics of wafers that were used for the fabrication of samples.* 31
Table 3.2: *Refractive indices of deposited films at 632 nm wavelength* [81]. 33
Table 4.1: *Labels of fabricated samples*. 42
Table 4.2: *The simulation results of J_{Gen} and losses caused by reflection and absorption for SiNA and SiNB* [85]. 42
Table 4.3: *The average results of fabricated cell samples.*.................................... 43
Table 4.4: *Sinton WCT-120TS measurement results of lifetime samples.* 43
Table 4.5: *Calculated hydrogen concentrations of deposited silicon nitride layers.* 57
Table 4.6: *Required times for association and dissociation of Fe_iB_s pairs for 0.2, 1.5 and 650 Ω.cm base resistivity groups.* 58
Table 4.7: *The concentration of Fe_i impurities at each ingot.* 59

LIST OF FIGURES

FIGURES

Figure 1.1: Market share of different wafer types, taken from the ITRPV 2023 report....2
Figure 1.2: PERC structure. 3
Figure 1.3: I-V graph with/without resistive effects. 4
Figure 1.4: Radiative recombination. 7
Figure 1.5: Auger recombination. 8
Figure 1.6: Shockley-Read-Hall recombination. 9
Figure 1.7: Interstitial and substitutional position of defects inside the Si bulk. 10
Figure 2.1: Three state model of B-O LID defects behavior. 14
Figure 2.2: Energy level of B-O defects and H atoms in the band gap diagram, taken from [13]. 16
Figure 2.3: Fractional H^0 concentration in p-type 1 Ωcm silicon substrate as a function of temperature and excess carrier concentration (Δn) by using Sah-Shockley statistics, taken from [32] 18
Figure 2.4: H charge state concentration according to fermi level A) at 300 °C and B) at 700 °C, taken from [67]. 23
Figure 3.1: PERC fabrication plan. 30
Figure 3.2: Wafer positions in the ingot. 31
Figure 3.3: Surface modification with KOH solution to form a pyramidal textured surface. 32
Figure 3.4: Fabrication plan of lifetime samples. 35
Figure 4.1: Degradation with light soaking of identically passivated 0.2 Ω.cm base resistivity samples with emitter, Group B and without emitter, Group D samples. 44
Figure 4.2: Degradation with light soaking of identically passivated 1.5 Ω.cm samples with emitter, Group F and without emitter, Group H samples. 45
Figure 4.3: Degradation with light soaking response of identically passivated 650 Ω.cm samples with emitter, Group K and without emitter, Group M samples. 46

Figure 4.4: Dark annealing enhanced degradation of identically passivated 0.2 Ω.cm samples with emitter, Group B and without emitter, Group D samples at 200 °C. 47
Figure 4.5: Dark annealing enhanced degradation of identically passivated 1.5 Ω.cm samples with emitter Group F and without emitter, Group H samples at 200 °C. 48
Figure 4.6: Normalized defect density of B-O defects for identically passivated Group D with 0.2 Ω.cm base resistivity and Group H with 1.5 Ω.cm base resistivity. LS1 is degradation after the initial condition while LS2 is degradation after dark annealing application, dashed lines are guide to eyes. 49
Figure 4.7: Optimization of B-O LID regeneration process on 0.2 Ω.cm samples of Group D with a constant illumination of 1-sun intensity and varying temperatures of 150, 170 and 190 °C. 50
Figure 4.8: Optimization of B-O LID regeneration process on 1.5 Ω.cm samples of Group H with a constant illumination of 1-sun. 51
Figure 4.9: Regeneration of cell samples of 0.2 Ω.cm base resistivity Group A and B passivated with SiNA and SiNB, and 1.5 Ω.cm base resistivity Group E and F passivated with SiNA and SiNB. 52
Figure 4.10: The effect of dark annealing enhanced B-O defect activation on LID regeneration on 1.5 Ω.cm samples of Group G with passivation of SiNA and Group H with passivation SiNB. 53
Figure 4.11: The results of laser hydrogenation with 915 nm diode laser under 124 ± 5 suns intensity of 0.2 Ω.cm base resistivity samples of Group C and D passivated with SiNA and SiNB. 54
Figure 4.12: The results of laser hydrogenation with 915 nm diode laser under 124 ± 5 suns intensity of 1.5 Ω.cm base resistivity samples of Group G and H passivated with SiNA and SiNB. 55
Figure 4.13: The average variation of base resistivity on 1.5 Ω.cm base resistivity samples symmetrically passivated with SiNA and SiNB by dark annealing at 190 °C for 9 hours. 57

Figure 4.14: LeTID response of Group G and Group H samples at 180 °C heat in a dark room.......60

LIST OF ABBREVIATIONS

ABBREVIATIONS

PERC: Passivated emitter and rear cell

CID: Current induced degradation

LID: Light induced degradation

LeTID: Light and elevated temperature induced degradation

Si: Silicon

Cz: Czochralski

SiN_x: Silicon nitride

Al_2O_3: Aluminum oxide

H: Hydrogen

P: Phosphorus

Ga: Gallium

B: Boron

O: Oxygen

ARC: Anti-reflective coating

SRH: Shockley-Read-Hall

IA: Illuminating annealing

LS: Light soaking

DA: Dark annealing

LIST OF SYMBOLS

SYMBOLS

E_c: valence band

E_c: conduction band

E_f: fermi level

η: efficiency

I_{sc}: short circuit current

J_{sc}: short circuit current density

I_0: saturation current density

FF: fill factor

V_{oc}: open circuit voltage

R_{sh}: shunt resistance

R_s: series resistance

n: refractive index

T: temperature

P_{MP}: maximum power point

N^*_{BO}: normalized boron-oxygen defect density

$[O_i]$: intrinsic oxygen concentration

$[B_s]$: substitutional boron concentration

τ_{eff}: effective lifetime

CHAPTER 1

INTRODUCTION

Today, one of the biggest challenges we face is climate change. Increasing CO_2 emissions causes detrimental side effects on our planet. Therefore, we need to prefer less or no carbon footprint methods in our daily lives. There are various sources of high carbon emissions, such as farming, non-renewable power plant sources, petrol cars, etc. Electricity generation and heating methods are mainly based on non-renewable sources such as coal, oil, and natural gas, causing the highest CO_2 emissions. Therefore, we must prefer less or no carbon footprint and renewable methods such as solar, wind, and tidal. Among them, solar energy has the highest potential and wide range of applicability for electricity generation.

Due to their low material cost and abundance, silicon-based solar cells are widely preferred by industry. Solar cells are a diode that contains a p-n junction structure. Under sunlight illumination, photons that have higher energy than the band gap energy of the silicon can generate an electron-hole pair by its absorption. Electricity can be generated by collecting those electrons and holes separately before their recombination.

The story of solar cells started in 1839 with Edmond Becquerel's demonstration of the photovoltaic effect for the first time. Then, in 1954, Bell Laboratories announced the first practical silicon solar cell. From the past to the present, different structured solar cells, such as Interdigitated back contact (IBC) cells, Passivated Emitter and Rear Contact (PERC), Tunnel Oxide Passivated Contact (TOPCON), etc., were

investigated. For the future, increasing solar cell usage can be a solution to reduce excess CO_2 emissions and protect our home planet Earth from climate change criris.

1.1 Czochralski Grown Silicon Wafers

Solar cells can be fabricated with various raw materials such as Ga, As, In, Si, etc. However, the solar cell industry is dominated by Si due to its abundance and cheap raw material prices [1].

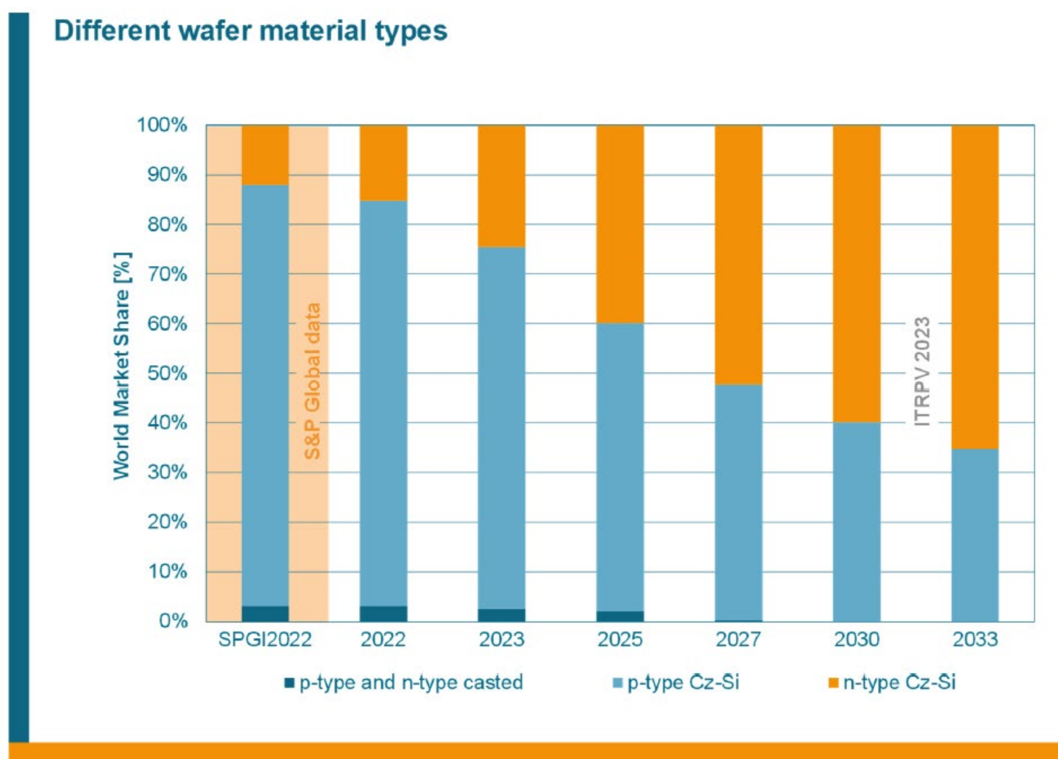

Figure 1.1: Market share of different wafer types, taken from the ITRPV 2023 report.

In the literature, various fabrication methods for silicon-based cells are available. The most known methods are Czochralski (Cz), Float Zone (FZ), and multi-crystalline (mc). As shown in *Figure 1.1*, Cz is the primary used method now and in the predictable future. However, Cz-Si has certain drawbacks, such as metallic impurities and oxygen contamination during Si ingot growth from quartz crucible

(SiO_2). These contaminations are known for their detrimental effect of degradation on solar cell parameters.

1.2 Passivated Emitter and Rear Cell (PERC)

As shown in Figure 1.2, PERC solar cell is a widely used solar cell structure that was first introduced by M. Green et al. in 1989 [2]. In this structure, the emitter region at the front side is formed by a doping process with the 5A group element of phosphorous (P) to create the required field effect for forming the p-n junction structure. Electrons are collected on the front side by the field effect, while holes are collected on the rear side. SiN_x at the front side for passivation of surface dangling bonds and anti-reflecting coating (ARC) feature is preferred. Also, SiN_x is used for the capping layer of deposited Al_2O_3 at the rear side. To generate electricity, ohmic contacts are formed at both the front and rear sides.

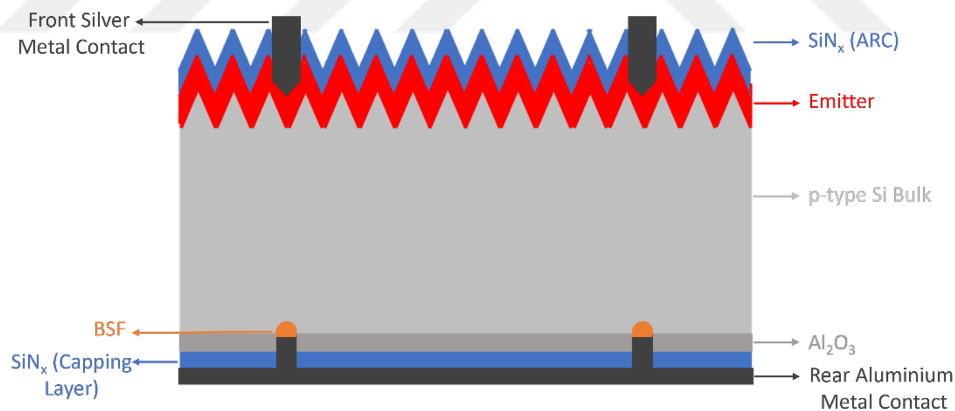

Figure 1.2: PERC structure.

1.3 Solar Cell Parameters

Characterization of solar cells with well-defined parameters has a critical role in identifying possible problems and focusing on their solutions. For example, the current (I) vs. voltage (V) graph can be used to define the behavior of a solar cell to determine parameters such as open-circuit voltage (V_{oc}), short-circuit current density (J_{sc}), fill factor (FF) and efficiency (η) [3].

1.3.1 Current vs Voltage Curve (I-V)

A solar cell is a diode with a p-n junction structure. However, instead of emitting light like LEDs, they absorb light and generate electron-hole pairs. The I-V graph of a solar cell represents the superposition of the cell diode in the dark with the light-generated current [4]. From the I-V graph of a solar cell, V_{oc} is the intercept of the y-axis, I_{sc} is intercept of the x-axis, and maximum power points can be extracted. Also, we can extract specific detrimental effects on a solar cell, such as shunt resistance (R_{sh}) [5] and series resistance (R_s) [6] from the I-V curve.

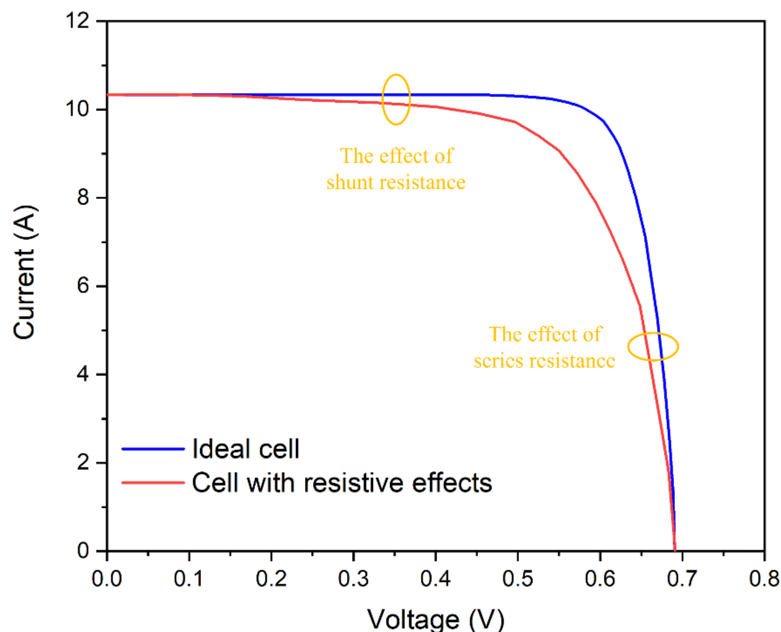

Figure 1.3: I-V graph with and without resistive effects.

As shown in *Figure 1.3*, the red line represents an ideal cell, whereas the black line represents a cell with resistive effects. From the figure, decreased squareness horizontally and vertically tells us about variations in series and shunt resistances.

Shunt resistance is resistance to current flow through an alternative way instead of the p-n junction in a cell, so high shunt resistance is desired in silicon solar cells. As shunt resistance decreases, an alternate path for current to flow becomes optional and reduces cell performance. Series resistance is resistance to current flow along the cell. Series resistance includes resistance caused by the silicon base, emitter, and metal contacts.

1.3.2 Open Circuit Voltage (V_{oc})

Open circuit voltage is the maximum possible voltage available from a solar cell at zero current conditions. V_{oc} corresponds to the forward bias on the cell due to light-generated current.

$$V_{oc} = \frac{nkT}{q} \ln\left(\frac{I_L}{I_0} + 1\right) \qquad \text{Eq. (1.1)}$$

Where n is the ideality factor, T is temperature, and I_L and I_0 are light generated and dark saturation currents. Although V_{oc} is expected to increase with increasing temperature, I_0 increases rapidly due to changes in intrinsic carrier concentration with increasing temperature.

1.3.3 Short Circuit Current (I_{sc})

A short circuit current is the maximum possible current that is available from a solar cell under short circuit conditions. During the illumination of the cell, electrons and holes are created by the absorption of incident photons. For an ideal solar cell, resistive effects can be ignored so it can be considered that no loss from resistive effects and short circuit current becomes the largest current value that can be generated. However, the usage of I_{sc} can cause troubles due to its dependency to the

area of solar cell. To overcome this problem, short circuit current density (J_{sc}) which is independent of the area of the solar cell can be used as in Eq.2.

$$I_{sc} = J_{sc}A \qquad \text{Eq. (1.2)}$$

$$J_{sc} = qG(L_n + L_n) \qquad \text{Eq. (1.3)}$$

J_{sc} is dependent on generation rate (G), electron and hole diffusion lengths (L_n, L_p) as shown in Eq.3.

1.3.4 Fill Factor (FF)

The fill factor is the measure of squareness of I-V curve for a solar cell. Higher squareness is desirable for better cell performance.

$$FF = \frac{P_{MP}}{V_{oc} * I_{sc}} \qquad \text{Eq. (1.4)}$$

FF can be defined by the ratio of maximum power that can be harvested from the solar cell to the product of open circuit voltage and short circuit current.

1.3.5 Efficiency (η)

Efficiency of a solar cell is commonly used and an easy-to-understand parameter that can give direct indication of cell performance. It is the ratio of power harvested from the solar cell to the incident power on it from the sun. Efficiency is dependent on variables such as intensity, spectrum of incoming light and temperature of the cell. Therefore, for the sake of comparison, efficiency is measured under conditions of AM1.5 and room temperature of 25 °C.

The incident power that can generate electricity is:

$$P_{max} = V_{oc}I_{sc}FF \qquad \text{Eq. (1.5)}$$

Where efficiency is:

$$\eta = \frac{V_{oc}I_{sc}FF}{P_{in}} \qquad \text{Eq. (1.6)}$$

1.4 Recombination

Under sunlight exposure, absorbed incoming photons with higher energy than the band gap of the silicon can create an electron-hole pair. By collecting electrons and holes separately before their recombination, electricity from a solar cell can be generated. Therefore, the recombination of electron-hole pairs is critical for solar cell performance. There are three main recombination mechanisms exist: Radiative, Auger, and Shockley-Read-Hall (SRH) recombination.

1.4.1 Radiative Recombination

Radiative recombination, also called band-to-band recombination, is commonly seen in direct band gap semiconductors.

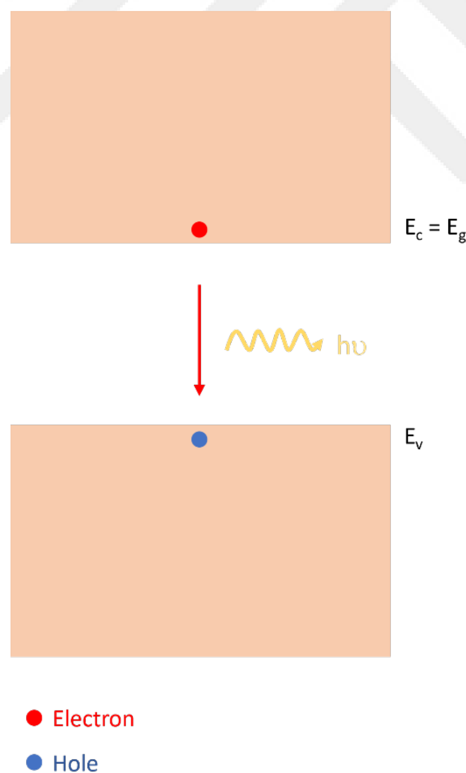

Figure 1.4: Radiative recombination.

As shown in *Figure 1.4*, when an electron in the conduction band (E_c) and a hole in the valence band (E_v) recombine, a photon that has similar energy with the band gap of the material is released. For example, LEDs are made of direct band gap materials such as GaAs, InGaN, AlGaAs, etc. Due to the indirect band gap characteristic of Si, radiative recombination has low effects on electron-hole pair recombination in Si-based solar cells, so that it can be neglected.

1.4.2 Auger Recombination

As depicted in *Figure 1.5*, Auger recombination occurs during the band-to-band recombination of electron and hole pairs, transferring excess energy to another charge carrier [7]. Then, this charge carrier goes to a higher energy level and thermalizes back to the edge of the conduction band by phonon interaction and heats the bulk.

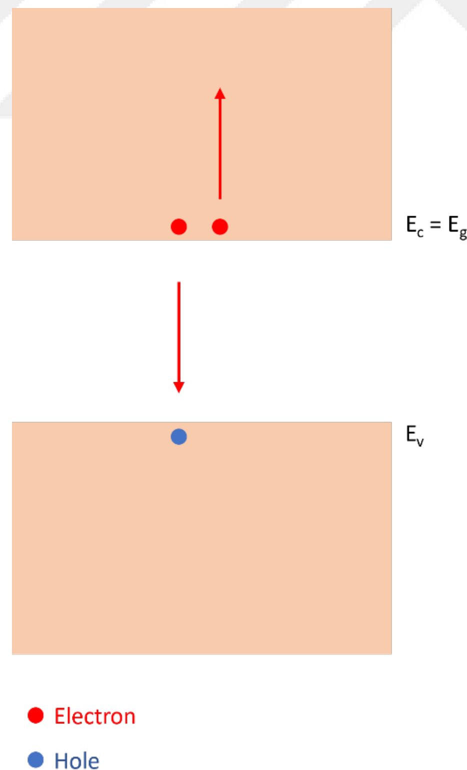

Figure 1.5: Auger recombination.

As the base doping level increases, the Auger recombination rate also increases. It predominantly affects carrier lifetime in highly doped silicon under low injection [8] and lowly doped silicon under high injection [9].

1.4.3 Shockley-Read-Hall Recombination

Shockley-Read-Hall recombination, also called recombination through defect levels, occurs by defect energy level or trap level in the band gap. The concentration of traps and impurities in the bulk is critical for the rate of SRH recombination mechanism. Therefore, crystallographic quality and the level of contamination have a high relation with SRH recombination.

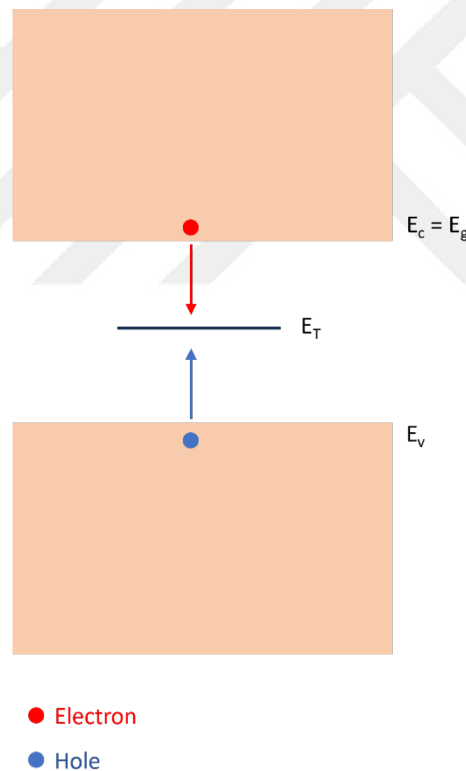

Figure 1.6: Shockley-Read-Hall recombination.

Electrons and holes can be trapped in the forbidden energy level between the band gap due to those traps and defect levels. As shown in *Figure 1.6*, if opposite charge carriers move up to the same recombination level before their thermal emission, then

they recombine. The energy level of the recombination site and its distance to the band edges affect the rate of carriers that move to that energy level. If the position of the recombination site is close to the band edges, they are less recombination active. Therefore, energy levels that are close to the mid-gap are highly recombinative.

1.5 Defects in the Bulk

Defects inside the bulk limit the performance of a silicon solar cell. Identifying those defects is critical to reduce their effects and improve the performance of cells. Defects inside the bulk are mainly positioned as substitutional sites or interstitial sites, as shown in *Figure 1.7*.

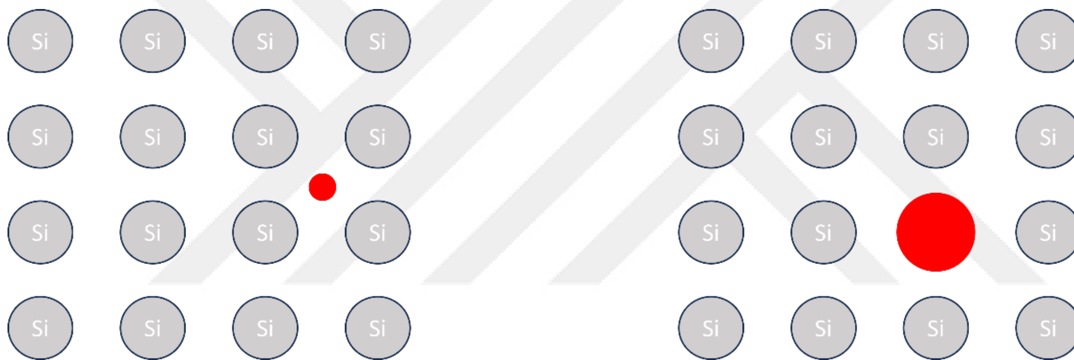

Figure 1.7: Interstitial and substitutional position of defects inside the Si bulk.

Defects inside the bulk can be categorized into intrinsic and extrinsic defects.

1.5.1 Intrinsic Defects

Intrinsic defects that are present in pure silicon without any extrinsic addition occur during the ingot growth process. Two commonly known intrinsic defects are vacancies and self-interstitials.

Vacancies are displaced atoms that are missing from the crystal lattice. When a vacancy exists, it leaves a hole behind it. Chemical reactions, radiation, or thermal energy can potentially create vacancy sites. Interstitials are atoms that are located in

between crystal lattices instead. When an atom is displaced from a crystal lattice to an interstitial position, it can form an interstitial with chemical reaction, radiation, and thermal energy. Vacancies and interstitials have the potential to interact with each other to form more complex defects. At room temperature conditions, the concentration of intrinsic defects is low. However, increasing temperature and doping level can increase its concentration.

1.5.2 Extrinsic Defects

During solar cell fabrication, the addition of dopants is required to increase the conductivity of silicon bulk and to form the required p-n junction. However, dopant atoms, called substitutional extrinsic defects, can replace silicon atoms at the crystal lattice. They can change the electronic property of the doped material, such as an n-type wafer by doping phosphorus or a p-type wafer by doping boron atoms. In other words, introducing dopant atoms is an impurity-introducing method. Some certain impurities during the ingot growth process contaminate the ingot. The common contaminants during the ingot growth are oxygen, carbon, iron, cobalt, etc. Those impurities have a detrimental side effect on silicon solar cell performance by behaving as recombination centers for capturing electrons and holes.

1.6 Motivation of Thesis

Solar cell installation has become increasingly popular to generate electricity for our daily needs. However, one of the main challenges after the installation is the degradation mechanisms of LID and LeTID that occur over time due to prolonged exposure to sunlight. Essentially, the efficiency of electricity generation decreases as the degradation phenomena elevates over time. LID is mainly caused by the activation of B-O complex during sunlight exposure. Hydrogen atoms can passivate those defects during the illuminated annealing process called regeneration. On the other hand, LeTID is caused by excess hydrogen atoms which interact with an

unknown complex. Although the exact mechanism of LeTID is still a mystery, applying low sun intensities with a specific heat or long duration of heat application can activate and then passivate the LeTID-originated complex. Therefore, hydrogen concentration inside the bulk is critical for both mechanisms.

The source of hydrogen inside the bulk is the silicon nitride passivation layer. According to the hydrogen concentration inside SiN_x the passivation of B-O defects can be enhanced, or LeTID-related degradation can be increased. Therefore, the characteristics of SiN_x layer have a critical importance. The base resistivity of a wafer is another crucial parameter for B-O defects. As the base resistivity of the wafer decreases, the concentration of the boron dopant atom increases. In other words, available boron atoms that can form B-O defects increase, and the extent of LID-related defects increases, too. For higher base resistivity samples, it is expected to observe fewer B-O defects.

Within this thesis, by using different base resistivity wafers from specially grown ingots, the effect of boron dopant concentration on the extent of LID was investigated. Also, two different SiN_x layers were deposited on identical samples to compare the effect of hydrogen concentration of passivation on LID. For LID passivation and degradation, two commonly known methods of halogen lamp with a hot probe and laser illumination were used. Optimization for a fast and effective way for LID passivation was investigated by comparing those methods. Moreover, the effect of hydrogen concentration on the extent of LeTID was investigated.

CHAPTER 2

THEORY AND BACKGROUND

Solar cell technology is critical in low or zero carbon emissions during electricity generation. Therefore, focusing on the problems of solar cells is crucial for further advancements and better cell performance. One of the critical challenges in Cz-Si p-type solar cells is degradation mechanisms.

Illumination of samples is a common method for activating degradation mechanisms. Any carrier injection method, such as illumination with sunlight, halogen lamp, laser, or forward-bias application, can cause the activation of those mechanisms. Therefore, Current Induced Degradation (CID) is a more appropriate way to name degradation mechanisms. However, Light Induced Degradation (LID) and Light and Elevated Temperature Induced Degradation (LeTID) are two commonly known mechanisms that are preferred to be called those names in academia and industry. In this thesis, LID and LeTID are used to define the degradation mechanism instead of CID. LID and LeTID are primarily responsible for performance losses in boron-doped p-type solar cells. LID can be observed in a short time scale, while LeTID can take years.

2.1 Light Induced Degradation (LID)

As mentioned in section 1.1, the Cz-Si growth method is commonly preferred for its low cost and easy production. However, one of the main drawbacks of the Cz method is the contamination of impurities to the ingot. Oxygen contamination occurs during the melting of silicon chucks at a quartz crucible and the growth of the ingot. The average oxygen contamination in p-type Cz-Si wafer is around $5 \times 10^{18} – 1 \times 10^{19}$

atoms/cm^3 [10]. Oxygen contamination during the Cz-Si growth technique is known for its degradation effects on cell performance. The commonly known LID degradation mechanism on p-type Cz-Si is caused by B-O defects/complex. After the fabrication of solar cells, during the first hours of sunlight exposure, B-O defects become active from an inactive state [11]. B-O complex activation is not caused by sunlight itself; instead, incoming photons that have higher energy than the band gap of Si generate excess charge carriers, and they cause degradation [12]. After the activation of those defects, a degradation of solar cell parameters such as Voc, Jsc, and η can be observed.

The first systematic description of LID mechanism was proposed by Hertguth et al. in 2006, called the three state model [11] as shown in *Figure 2.1*.

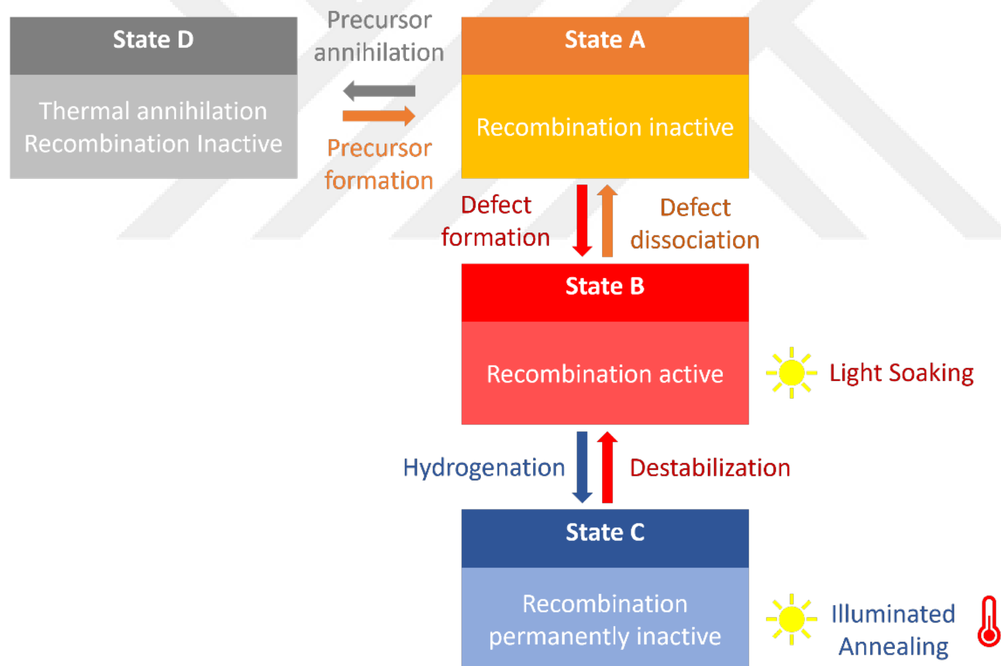

Figure 2.1: Three state model of B-O LID defects behavior.

This model has three main states for B-O defect behaviors. In State A, B-O defects are assumed to be inactive, so they cannot cause any performance loss. In State B, B-O defects become recombination active with sunlight exposure or carrier injection. Therefore, B-O defects inside the bulk cause degradation of solar cell parameters.

Lastly, State C indicates the passivation of B-O defects and recovery from the degraded state. At that state, B-O defects are stable for the rest of its time, even under light soaking application. The main role of the passivation of B-O defects can be attributed to the hydrogen (H) atoms inside the bulk. Lastly, an additional state of State D, shown in *Figure 2.1*, was proposed for the thermal precursors. State D represents B-O defect precursors, which are annihilated thermally [13]. During intermediate temperature processing, precursors form with the reaction from state D to A. By high-temperature application, a reaction occurs from state A to D by precursor annihilation. The concentration of active B-O defects in a wafer has a direct relation with the thermal history of the wafer [14]. For example, by the variations in the recipe of the firing step for contact formation, the change in the permanent recovery rate of B-O defects during the illuminated annealing process can be observed [15]. However, the thermal deactivation of B-O defects is a different mechanism compared to the regeneration process by illuminated annealing [16].

2.1.1 B-O Defects

Boron and oxygen atoms are introduced into the bulk during Cz-Si ingot growth. While B atoms are positioned in the substitutional site and negatively charged, oxygen atom impurities are placed in interstitial sites and positively charged. In the literature, B-O defects are reported to exist in the form of substitutional boron (B_s) that captures fast diffusing oxygen dimers (O_{2i}), which is a metastable B_sO_{2i} complex [17]. Normalized defect density (N^*_{BO}) can indicate quantitative estimation of B-O complex concentration. From Hamer et al. [18], N^*_{BO} can be calculated by:

$$N_{BO}^{*} = \frac{1}{\tau_{eff}} - \frac{1}{\tau_{eff_{DA}}} \qquad \text{Eq. (2.1)}$$

where τ_{eff} is extracted lifetime at any condition and $\tau_{eff_{DA}}$ is effective lifetime after dark annealing (DA).

According to work performed by Glunz et al., varying [O_i] has a specific effect on the concentration of B-O complex more than the boron doping level [14]. In fact,

N^*_{BO} scaling is roughly quadratic with [O_i] [19], [20]. Also, there is a strong dependence between N^*_{BO} and boron base doping concentration, which has approximately linear scaling [20]–[22]. Therefore, decreasing [O_i] and boron doping levels to lower concentrations would be critical for reducing B-O LID.

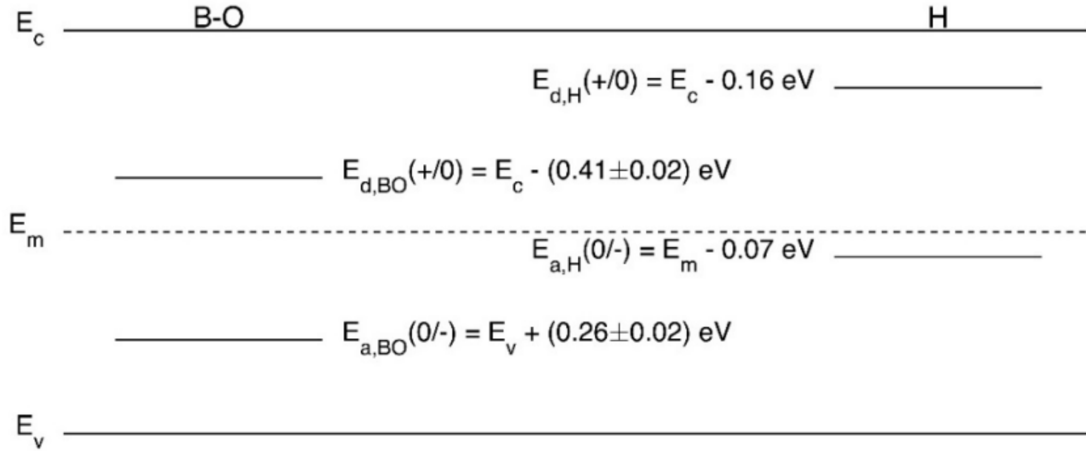

Figure 2.2: Energy level of B-O defects and H atoms in the band gap diagram, taken from [13].

As shown in *Figure 2.2*, charge states for both B-O complex and hydrogen are shown. Although the negative U-impurity feature of hydrogen is widely known, the charge states mechanism of B-O defects is still unclear. In the literature, the positive charge state of B-O complex is $E_C - 0.41$ eV with a k value of 9.3 is well known and measured [23], [24].

2.1.2 Passivation of B-O Defects

According to section 2.1, for the transition from State B, the degraded state, to State C, permanent recovery from the degraded state, B-O LID complex can be permanently deactivated by an illuminated annealing application [11]. Hydrogen is known for its ability to permanently passivate the B-O LID complex by changing its charge state during the illuminated annealing [25]. After the permanent deactivation process, further degradation caused by B-O LID is not expected to be observed for additional illumination to the sample. The concentration of H inside the bulk is

critical for effective passivation. If a lower concentration of H is introduced to the bulk, passivation can be challenging due to fewer hydrogen atoms and a higher concentration of defects and impurities, such that degradation can occur with illumination by activation of B-O defects.

As depicted in section 2.1.1, B-O complex is mainly positively charged with the energy level of E_C – 0.41 eV. The hydrogen atom inside the Si bulk has a negative U-impurity feature, which means hydrogen can exist in the bulk at three different charge states (H^-, H^0, H^+) simultaneously [26]. Each hydrogen species has a different diffusion velocity inside the p-type bulk due to coulombic forces. According to the reported diffusivity values of other hydrogen species at 150 °C, H^0 has a diffusivity value ~1.5 orders higher than H^- while H^- has ~2.5 orders higher diffusivity than H^+ [27]. On the other hand, in the work performed by Rizk et al., H^0 has the lowest diffusivity at the temperature level of 120 °C – 180 °C [28]. Thus, the literature has uncertainty on the characteristics of hydrogen atom species.

The doping type of the bulk determines the majority charge state concentration of hydrogen inside the bulk. If bulk is p-type, the major hydrogen charge state species is H^+; if bulk is n-type, the major hydrogen charge state species is H^- [29]. Therefore, in p-type samples, H^+ will be the majority charge state, and we need to passivate BO^+ complex. Due to coulombic forces, BO^+ complex repels the most abundant charge state of H^+ and cannot react with it, so B-O LID cannot be passivated. The solution to this problem is increasing the H- or H0 concentration inside the bulk.

H^- can easily passivate BO^+ defects thanks to its high reactivity rate in silicon substrate [25]. Temperature and Δn are critical for the concentration of H^0 inside the bulk and to passivate defects. Therefore, according to Figure 2.3, appropriate conditions to increase H^0 can be achieved by applying a certain level of heat and carrier injection. Although increasing the temperature of a silicon substrate with constant carrier injection can provide a certain amount of H^0, high thermal budget applications are known for their detrimental side effects on silicon solar cells, so applying reasonable thermal budget applications is preferred. On the other hand,

increasing Δn with constant temperature also provides a certain amount of H^0 with constant temperature. Thus, applying both high carrier injections with reasonable thermal application seems best. Therefore, illuminated annealing, widely performed by a halogen lamp and the hot plate, is preferable and commonly used in the literature [30], [31].

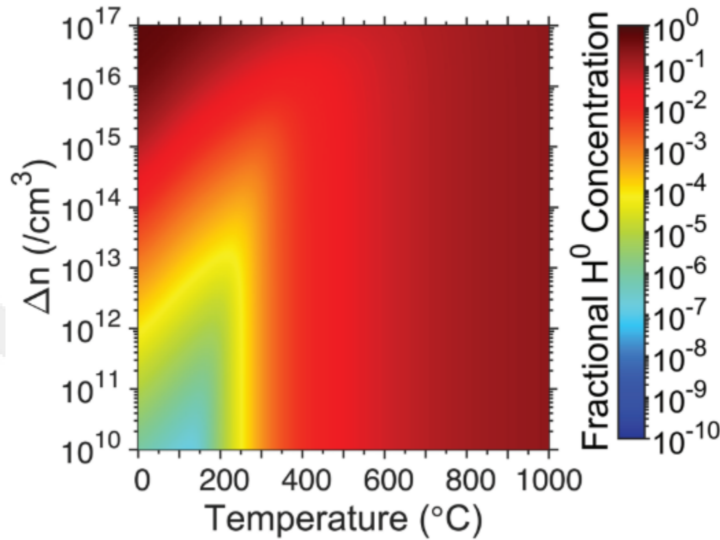

Figure 2.3: Fractional H^0 concentration in p-type 1 Ωcm silicon substrate as a function of temperature and excess carrier concentration (Δn) by using Sah-Shockley statistics, taken from [32]

A halogen lamp is a practical method to mimic the sun spectrum easily due to its working principle. Also, laser illumination [33]–[36] or forward bias application under a specific temperature [37]–[39] is applicable for the regeneration process of B-O LID defects. Forward bias application with applied heat is commonly preferred in mass production due to its short application duration and mass production compatibility [39]. Laser illumination is a new method that uses a specific wavelength to illuminate the sample. It is a promising way to deactivate the B-O complex permanently in seconds. A laser can provide an excess number of photons with a specific wavelength to a particular area. As the intensity of light increases, Δn can increase drastically, and the temperature of laser illumination applied to regions increases, too. Therefore, laser illumination is a potentially fast and easy application method for regeneration. There are new attempts to integrate the laser illumination

method into mass production lines by replacing them with current and heat applications.

2.1.3 The Effect of Base Resistivity on LID

The base resistivity is the inverse of the conductivity of the silicon bulk. Adding boron for the p-type wafer or phosphorous for the n-type wafer increases the conductivity of the bulk. In low bulk resistivity samples, Auger recombination becomes the dominant effect, and it increases as base resistivity decreases. Moreover, as we know from section 2.1.1, B-O LID complex concentration has a linear dependence on [B_s]. Therefore, increasing boron concentration increases B-O LID-related degradation [21]. This is one of the reasons why lowly doped silicon substrate is commonly preferred for high-efficiency solar cell applications. Thus, according to the base resistivity of the wafer, the extent of B-O LID degradation should be considered for determining the duration of illuminated annealing for permanent deactivation.

2.1.4 Fe-B Pairs

Apart from oxygen atoms that cause B-O LID, iron atoms that form Fe_iB_s pairs are also known for their detrimental effects on cell parameters, which is a LID. Iron is a commonly faced contaminant in Cz-Si grown wafers with a concentration of 1 x 10^{11} cm^{-3} for non-gettered wafers [40]. Interstitial iron (Fe_i) is known for its high recombination active characteristic that can cause performance loss in cell parameters [41] with the fermi level energy of E_V + 0.387 eV and capture cross section ratio of $k = E_V + 0.38\, eV$. In p-type wafers, iron exists in unbounded interstitial form under excess carrier injection conditions such as illumination [42]. On the other hand, in the darkness, due to the positive charge of Fe_i^+, it tends to combine with negatively charged dopant atoms, e.g., B and Ga [43]. To calculate the

time requirement for the association of Fe_iB_s pairs under dark storage after excess carrier injection to dissociate them, the following formulas can be used:

$$\tau_{assoc} = 5\ x\ 10^{15}\ x\ \left(\frac{T}{N_A}\right)\ x \exp\left(\frac{0.66}{kT}\right) \qquad \text{Eq. (2.2)}$$

where k=8.617 x 10^{-5} eV/K and T in Kelvin at 30 °C room temperature, N_A is dopant concentration and τ_{assoc} is the required time for association [44].

$$[Fe_i]_{(t)} = [Fe_i]_{(t=0)}\ x \exp\left(-\frac{t}{\tau_{assoc}}\right) \qquad \text{Eq. (2.3)}$$

Fe_i and Fe_iB_s has a distinct recombination property from each other due to the difference in their electron to hole capture cross-sections, which is higher for Fe_i [41]. To quantify the concentration of Fe_i injection-dependent lifetime measurement can be used [45]. Firstly, by excess carrier injection e.g., illumination long enough to dissociate the Fe_iB_s pairs and measuring the samples. However, to obstruct any further effect other than Fe_i, the temperature of the sample during the illumination is critical. If the heat of the sample exceeds the temperature range of 50 °C, the base resistivity of the sample can vary, which has the potential to effect lifetime results to cause deflections on the calculations. Secondly, by keeping samples in the dark for a sufficiently long time to let enough time for the formation of Fe_iB_s and measuring. Another key point for the dissociation of the Fe_iB_s pairs is the increase in lifetime values. As they dissociate, the effective lifetime values increase due to difference of capture cross sections of Fe_i and Fe_iB_s. A certain quantification for $[Fe_i]$ can be done by comparing injection dependent lifetime results.

$$[Fe_i] = C\left(\frac{1}{\tau_{light}} - \frac{1}{\tau_{dark}}\right) \qquad \text{Eq. (2.4)}$$

where τ_{light} is carrier lifetime after light soaking to dissociation Fe_iB_s which Fe_i, becomes dominant and τ_{dark} is carrier lifetime after dark storage to associate Fe_iB_s pairs which Fe_iB_s is dominant. The constant C dependent on dopant concentration,

temperature, and carrier injection. To calculate constant C, the following formula can be used [46]:

$$C\ (\Delta n) = \frac{1}{X^{Fe_i} - X^{FeB}} \qquad \text{Eq. (2.5)}$$

$$X^{Fe_i} = \frac{v_{th}\left(N_A + \Delta n_{Fe_i}\right)}{\left(\frac{1}{\sigma_n^{Fe_i}}\right)\left(N_A + p_1^{Fe_i} + \Delta n_{Fe_i}\right) + \left(\frac{\Delta n_{Fe_i}}{\sigma_p^{Fe_i}}\right)} \qquad \text{Eq. (2.6)}$$

$$X^{FeB} = \frac{v_{th}(N_A + \Delta n_{FeB})}{\left(\frac{1}{\sigma_n^{FeB}}\right)(N_A + \Delta n_{FeB}) + \left(\frac{1}{\sigma_p^{FeB}}\right)(n_1^{FeB} + \Delta n_{FeB})} \qquad \text{Eq. (2.7)}$$

where Δn_{Fe_i} and Δn_{FeB} are measured excess carrier densities in states of Fe_i and Fe_iB_s. v_{th} is thermal velocity, N_A is acceptor dopant concentration. $\sigma_n^{Fe_i}$ and $\sigma_p^{Fe_i}$ are capture cross sections. $p_1^{Fe_i}$ is SRH density for hole in the state of Fe_i and n_1^{FeB} is SRH density of electrons for the state of Fe_iB_s. The values of v_{th}, $\sigma_n^{Fe_i}$ and $\sigma_p^{Fe_i}$ can be found from the literature.

2.1.5 Passivation of Fe-B Pairs

Hydrogen atoms are known for their ability to passivate Fe_i atoms inside the bulk. Although the exact mechanism has not been found yet, according to the work done by Kouketsu et. al., DLTS peak reduces or disappears by introducing hydrogen into the bulk [47]. It is considered that, positively charged interstitial iron atoms (Fe_i^+) can bond with H^- atoms and form Fe-H pairs and become recombination inactive [47], [48]. However, no evidence has been found for such pairs yet [47]. In the literature, apart from the Fe-H bonds, another alternative explanation for mechanism for the reduction of $[Fe_i^+]$ impurities were proposed. Instead of Fe-B pair formation to explain the decrease in $[Fe_i^+]$, they indicate that due to increased diffusivity of

metallic impurities during the hydrogen introducing method or annealing the sample in a hydrogen ambient, the diffusivity of metallic impurities increases towards to the surface [49], [50].

2.2 Light and Elevated Temperature Induced Degradation (LeTID)

After the investigation of LID, we can move into the next critical degradation mechanism of LeTID. The main difference between LeTID from LID is its dynamics and the duration of degradation. LeTID was first observed by Ramspeck et al. on mc-Si solar cells in 2012 [51]. LeTID is known for its long-time duration requirement to cause degradation on cell parameters [52]. LeTID can be activated by both illuminated annealing at low temperatures or annealing in the dark [53]. However, it is suspected that the LeTID mechanism for both techniques can be different from each other. Except from LID, LeTID is independent of base doping species and their concentrations so it can be observed in n-type [54], Cz-Si [55] and FZ-Si [56] samples. Existence of hydrogen atoms inside the bulk is known enough for LeTID to occur so far [57]. For example, in n-type wafers, there is no boron atom inside the bulk to cause B-O LID, but we can see its degradation by applying appropriate conditions for LeTID [54]. The concentration of hydrogen in the bulk is critical for LeTID [58]. Excess interstitial hydrogen atoms do not speed up the recovery rate as in LID, instead, it causes elevated degradation of cell parameters caused by LeTID [59]. Also, the effect of peak firing temperature was observed in samples fired with hydrogen-rich passivation layers. The extent of degradation caused by LeTID increases with the increasing peak firing temperature [60]. The reason is hydrogen diffusion from SiN_x:H layer to the bulk is a temperature dependent process [61]. Although many recent studies showed that the involvement of hydrogen atoms inside the bulk is a root cause of LeTID, its mechanism has not understood yet [62], [63].

2.3 Hydrogen Atoms Inside the Bulk

In silicon bulk, hydrogen atom has low solubilities while it has fast diffusivity [64]. However, in the temperature range of T = 300-600 K, diffusivity of H atoms can be reduced by trapping effects [65]. Hydrogen inside the silicon bulk is known for its negative U impurity characteristic [26]. In other words, H^+ donor level is positioned above the H^- acceptor level. Hydrogen atoms can exist in all $H^+/H^-/H^0$ charge states at the same time inside the silicon bulk. Also, hydrogen species are highly active in the interaction of differently charged defects. Due to this characteristic of hydrogen, it can combine all types of defects if its charge state is appropriate for the bonding. Moreover, atomic hydrogen is known to be able to passivate shallow acceptors and donors by forming neutral recombination complexes [66].

According to *Figure 2.4,* the concentration of H^0 increases with increasing temperature just as in *Figure 2.3*. When the position of E_f is above the mid-gap, H^- will be the dominant species while if the mid-gap is below as in p-type Si, H^+ will be the dominant species. [26].

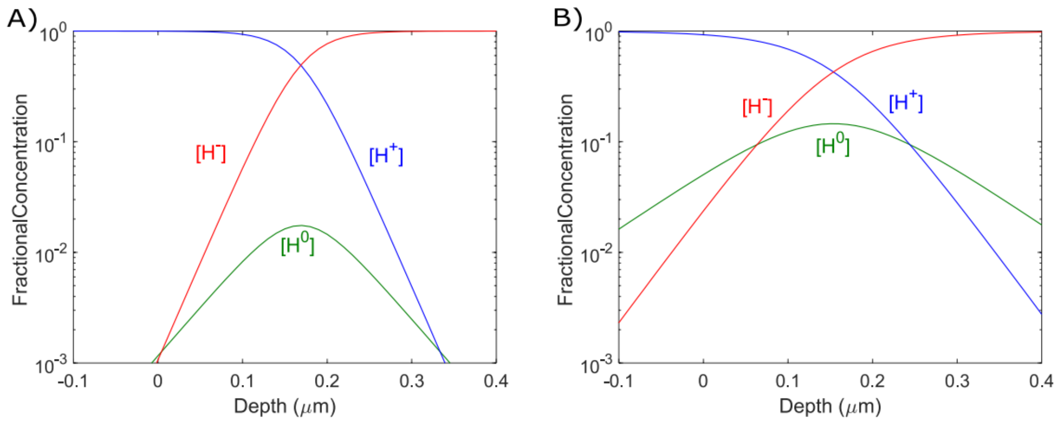

Figure 2.4: H charge state concentration according to fermi level A) at 300 °C and B) at 700 °C, taken from [67].

Thus, hydrogen species are highly affected by the doping type of the silicon bulk and turns its charge state accordingly due to fermi energy level. The lowest concentration of hydrogen charge state candidate is H^0 at both types of bulk at the equilibrium. Due

to the neutral charge state of H^0, its motion inside the bulk is easiest because it is unaffected by electric fields inside the bulk. Also, H^0 is highly active because it can bond with both positively charged defects and negatively charged states by giving or taking one electron and changing its charge state. Therefore, the amount of H^0 concentration is very critical for the defect passivation in all types of bulk. However, under normal conditions, H^0 is not thermally stable so it cannot maintain its existence too long, it can only be observed under nonequilibrium condition [68]. Therefore, with an additional application which is called illuminated annealing, H^0 concentration inside the bulk can be increased. Then, the ability of defect passivation can be enhanced. Thus, for the hydrogen included mechanisms such as LID and LeTID, carrier injection and thermal applications (firing and cooling) are critical. However, those application also can cause new problems as hydrogen induced contact resistivity that is increased by counter doping of contacts with H atoms [69], [70].

2.3.1 SiN_x:H Passivation Layer

SiN_x:H is widely used passivation layer in solar cell industry for its ability to passivate inter layer dangling bonds passivation and being hydrogen source for defect passivation. SiN_x dielectric layer can be deposited by various methods such as PECVD, LPCVD and ALD. In the literature, PECVD deposited SiN_x:H is widely preferred in both industry and research centers.

In LID and LeTID, hydrogen atoms have critical effect on both regeneration and degradation mechanisms. Hydrogen atoms inside the bulk have a positive effect to passivate B-O defects permanently for LID. Also, it can passivate metallic impurities and various defects in the bulk. On the other hand, in LeTID mechanism, hydrogen atoms inside the bulk causes degradation in the long term on solar cell parameters. Therefore, hydrogen concentration inside the bulk is very critical for the passivation of LID and LeTID originated defects.

The main source of H inside the silicon bulk is SiN_x:H passivation layer. During the firing step, hydrogen atoms inside the SiN_x:H layer starts to effuse to the environment and diffuse into the bulk [71]. Hydrogen diffusion inside of the bulk can be manipulated by peak firing temperature, furnace belt speed, SiN_x:H stoichiometry etc. Although an increase in hydrogen concentration inside the bulk would be beneficial to the passivation of bulk defects [72], it can cause detrimental damages to the bulk by forming LeTID-related defects in long term [73]. The concentration of hydrogen atoms that diffused into bulk is around 10^{14} - 10^{15} cm^{-3} [74]. Hydrogen concentration of an SiN_x layer can be determined by its refractive index. As the refractive index increases, the concentration of [Si-H] bonds increase [75]. Due to the increased silicon content in SiN_x layer, atomic density decreases, and it provides increasing hydrogen diffusivity. Thus, hydrogen diffusion to the bulk from the passivation layer can be enhanced [75].

2.3.2 Hydrogen Diffusion Mechanism

Hydrogen diffusion to the bulk from SiN_x:H layer has critical role on passivation of surface dangling bonds and bulk defects. During the diffusion of hydrogen, it can face with various layers (e.g. passivaiton layer, emitter, surface and bulk defects) that can effect the diffusion.

For example, highly doped emitter layer can trapped hydrogen due to dopant bonding [67]. Therefore, emitter doping concentration and even emitter profile has a critical role for the hydrogen diffusion [76]. Also, defective regions and impurities can associate with hydrogen atoms to trap them. When those regions collects hydrogen atoms around themselves, they can behave as secondary hydrogen sources by postannealing applications and they can enhance the hydrogen diffusion inside the bulk [77].

Hydrogen atoms can be affected by E-fileds easily according to their charge states. Especially, during the diffusion of hydrogen atoms from SiN_x:H layer to the bulk

through p-n junction, they should change their charge states from H^- to H^+ for significant transport in p-type bulk with n^+ doped emitter samples (e.g. p-type PERC) [67]. On the other hand, under illumination and temperature applications, hydrogen atoms were observed to move towards the surface of the samples by the effect of the E-filed effect created by the p-n junction [29].

Hydrogen diffusion can be retarted due to base dopants atoms relations (B-H and P-H bonds) and formaion of H_2 molecules [27].

$$H^{+} + B^{-} \leftrightarrows BH \qquad \text{Eq. (2.8)}$$

$$H^{-} + P^{+} \leftrightarrows PH \qquad \text{Eq. (2.9)}$$

with rate coefficients k_{BH} and k_{PH} which are:

$$k_{BH} = 4\pi r_C D_{H^+} \qquad \text{Eq. (2.10)}$$

$$k_{BH} = 4\pi r_C D_{H^-} \qquad \text{Eq. (2.11)}$$

where D_{H^+} and D_{H^-} are diffusivities of H^+ and H^- and r_c defines a radius for the capture in according to coulombic interaction.

2.3.3 Base Resistivity Variation by B-H Bonds

Base resistivity of a silicon ingot is determined by the addition of dopant materials such as B, P and Ga. However, the resistivity of the wafer can be increased by the hydrogen bonding with the dopant atoms such as B-H bonds in p-type bulk and P-H bonds in n-type bulk due to deactivation of dopant atoms [74]. The variation in base resistivity can be measured so the formation and dissociation of B-H or P-H bonds can be followed [78].

According to work done by Voronkov et. al. [79],

$$\frac{d[H_{2A}]}{dt} = -\propto_A \left(p \times [H_{2A}] - X_A \frac{\left(\frac{[BH]}{[B]}\right)^2}{p} \right) \quad \text{Eq. (2.12)}$$

where $[H_{2A}]$ is hydrogen dimer concentration, $[B]$ is boron atom concentration that is not passivated by hydrogen atoms, [BH] is the concentration of boron atoms passivated with hydrogen, $\propto_A$ is rate of dissociation coefficient of $[H_{2A}]$ dimers, p is hole concentration and X_A is the modified equilibrium constant. The values of $\propto_A$ and X_A can be calculated according to Voronkov *et. al.*, by using the following formulas of [79]:

$$\propto_A = (1.3 \times 10^{-6}\ cm^3 s^{-1}) \exp(-1.3\ eV/kT) \quad \text{Eq. (2.13)}$$

$$X_A = (2.35 \times 10^{66}\ cm^{-9}) \exp(-1.7\ eV/kT) \quad \text{Eq. (2.14)}$$

Where, k is the boltzman constant while T is the temperature of applied heat treatment in Kelvin.

$$[BH] = p - p_0 \quad \text{Eq. (2.15)}$$

$$[B] = N_B - [BH] \quad \text{Eq. (2.16)}$$

Where p_0 is hole concentration before firing, p is current hole concentration and N_B is the total boron concentration.

After heat treatment, there will be a equilibrium state in between $[H_{2A}]$ and [BH] which equilibrium can be described by:

$$[H_{2A}] = X_A \frac{\left(\frac{[BH]}{[B]}\right)^2}{p^2} \quad \text{Eq. (2.17)}$$

Thus, to calculate total hydrogen concentration, the following formula can be used:

$$[H_{tot}] = 2 \times [H_{2A}] + [BH] = 2 \times X_A \frac{\left(\frac{[BH]}{[B]}\right)^2}{p} + [BH] \quad \text{Eq. (2.18)}$$

CHAPTER 3

EXPERIMENTAL

In this thesis, the extent of LID which is directly dependent on the boron base dopant concentration and its passivation rate varies with hydrogen concentration inside the bulk was investigated. Also, the effect of bulk hydrogen concentration on LeTID effect researched. For this purposes, two different SiN_x:H passivation layer was deposited on samples which have the base resistivity values of 0.2, 1.5, and 650 Ω.cm to compare their effects on both LID and LeTID mechanisms.

Lifetime sample fabraication is a useful method to inestigate lifetime of charge carriers, recombination mechanisms and material quality which does not require any metallization process. Therefore, lifetime samples with symmetrical passivation layer and symmetrical emitter and passivation layer samples were fabricated in addition to PERC. While only LID testing conditions were applied to investigate cells, in lifetime samples, both LID and LeTID effects were investigated. For the fabrication of cell samples, the PERC structure was preferred for its well-known design and state-of-the-art level of knowledge in ODTÜ GÜNAM.

3.1 PERC Sample Fabrication

The fabrication plan for PERC is shown in *Figure 3.1*.

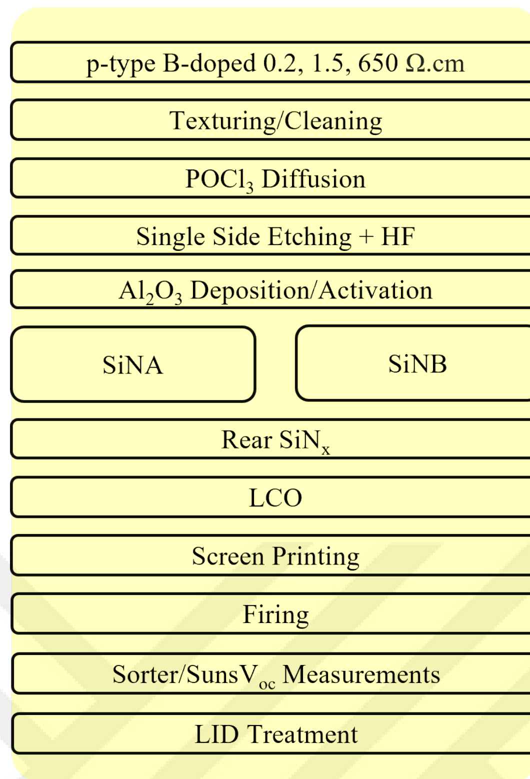

Figure 3.1: PERC fabrication plan.

First, as cut wafers were textured to form pyramidal shapes to reduce reflection on the surface of the wafer. Then, they were applied to a diffusion process to form the required p-n junction. After a single side etching of the rear side of the wafer to remove unwanted diffused phosphorus atoms, Al_2O_3 layer was deposited to the samples by an atomic layer deposition device. Front dielectric with two different recipes of SiNA and SiNB and rear dielectric layers were deposited by PECVD, and ablation for LCO was done with a picosecond laser. Finally, samples were screen-printed and underwent the firing process.

3.1.1 Characteristics of Wafers

In this study, 158.75 x 158.75 mm^2 (G1) size samples with base resistivities of 0.2, 1.5, and 650 Ω.cm were laser cut by a nanosecond marker laser to 156.75 x 156.75 mm^2 (M2) size and were used as substrates. Ingots had been growth in KALYON

PV facility. Each base resistivity group was selected from the same ingot position, C, as shown in *Figure 3.2*.

The reason for laser cutting is that the ODTÜ GÜNAM Photovoltaic Line (GPVL) able to process M2-size wafers. Three different wafer groups were selected according to their base resistivities and ingot positions, are shown in Table 3.1.

Table 3.1: *Characteristics of wafers that were used for the fabrication of samples.*

Dopant	**Base Resistivity (Ω.cm)**	**Ingot Positions**	**Wafer Thickness (µm)**
B	0.2	C	170 ± 10
B	1.5	C	170 ± 10
B	650	C	170 ± 10

During the growth of the Cz-Si ingot, [O_i] levels vary along the ingot position, as shown in *Figure 3.2* from T to A, which oxygen concentration is lowest at the section T and it increases along A [80]. Therefore, the ingot position of the wafer is an important parameter that can potentially affect the degradation level. All wafers were chosen from the exact position of ingots, and each group of wafers was chosen as sister wafers for the sake of comparison.

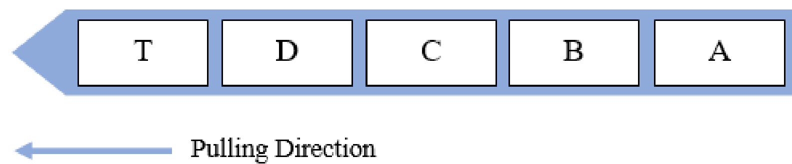

Figure 3.2: Wafer positions in the ingot.

3.1.2 Samples Surface Morphology Modifications

After the ingot growth process, the wire sawing process with a special wire coated with diamond or silicon carbide particles is used to have thin slices of ~170 µm thickness as-cut wafers.

Figure 3.3: Surface modification with KOH solution to form a pyramidal textured surface.

For the surface modification, as-cut wafers were exposed to the texturing process by a mixture of KOH, deionized water (DI), and monoTEX additive solution in Rena BatchTEX tool to increase the light trapping and reduce the reflection from the surface by forming random pyramidal morphology on the surface of the wafer. KOH is a commonly known chemical for its anisotropic etching characteristic widely preferred in Si etching processes. KOH has specific etching rates that depend on the crystal plane directions, creating a pyramidal structure with a height of 2-3 µm as shown in *Figure 3.3*. Following the texturing process, wafers were exposed to ozone and HF cleaning.

3.1.3 Emitter Formation

The emitter formation, called the doping process, was applied to form an n^+ region at the front side of the samples for the required p-n junction. For emitter formation, liquid $POCl_3$ source was used under atmospheric conditions with N_2 and O_2 precursors. Then phosphosilicate glass (PSG) forms on both surfaces, and phosphorous atoms inside the glass layer are driven into the Si bulk at high-temperature drive-in application, resulting in the sheet resistance of ~90 Ω/□ with 0.3-0.5 µm thickness.

Following the emitter formation, the rear side of the wafer underwent the single-side etching (SSE) process in Rena Inpilot device to remove rear-side doping. Rear side emitter removal was critical due to the collection of electrons from the n^+ region at the front side and holes at the rear side effectively to generate electricity from solar cells by p-n junction structure.

3.1.4 Al_2O_3 Deposition

Al_2O_3 is a widely used rear side passivation layer in PERC fabrication. The ALD method was used for its high-quality passivation ability and high control of deposition thickness for Al_2O_3 deposition. While the aluminum precursor trimethylaluminum (TMA) was used, DI water was preferred as the O precursor. At 200 °C, the sample went forward and back at the reactor zone until 5 nm Al_2O_3 layer formation with ~0.13 nm deposition thickness at each cycle. After the Al_2O_3 deposition, it was exposed to the annealing process in an annealing furnace at 425 °C for 15 minutes under N_2 ambient for its activation and degassing to prevent it from blistering.

3.1.5 SiN_x Deposition

For the deposition of SiN_x:H layer, an industrial-size PECVD system at low frequency was used. Passivation layers were deposited with varied flow rates of NH_3, N_2O, N_2 and SiH_4 gasses at 170 Pa and 450 °C.

Table 3.2: *Refractive indices of deposited films at 632 nm wavelength* [81].

Recipe Name	Refractive Index (n)	Thickness (nm)
SiNA	2.04	95
SiNB	2.18	95
SiNC	1.96	55
SiO_xN_y	1.73	20

Two different passivation layers, SiNA and SiNB, were preferred for front side passivation to investigate the effect of varied SiN_x:H layers on degradation and regeneration processes. By varying the flow of gases, hydrogen concentrations inside the dielectric layers and refractive indices were varied. The rear side capping layer of SiN_x layer was kept identical.

3.1.6 Laser Contact Opening (LCO)

For the local ablation of rear dielectric layers of PERC samples to form rear metal contacts, the wavelength of 532 nm picosecond laser was used.

3.1.7 Screen Printing

For the metallization process, the screen-printing method was used. For the front side, 129 fingers 5 busbar structure with fire through silver (Ag) paste was used to form front contacts during the firing step while the rear side was printed fully with non-fire through Al paste, which only 3% is in contact with Si-bulk. The metal fraction at the front side is 4.4%, with a cell area of 244.3 cm^2.

3.1.8 Firing

After the screen-printing of samples, they were exposed to firing steps to form contacts. During the firing, diffusion of hydrogen atoms from the SiN_x:H layer to the bulk for passivation of interface defects and bulk defects occurs. An industrial firing recipe for PERC was preferred to investigate hydrogen diffusion under the same conditions among different SiNA and SiNB.

3.2 Lifetime Sample Preparation

In section 3.1, the general process flow for PERC fabrication is given. Two different groups of lifetime samples are named front emitter and front, which are symmetrically fabricated with emitter and front surface passivation and only front surface passivation without emitter identical to layers used in PERC fabrication. In the Front group, the only difference with Front Emitter was the existence of emitter. They identically passivated with the front passivation layer of the PERC group without an emitter.

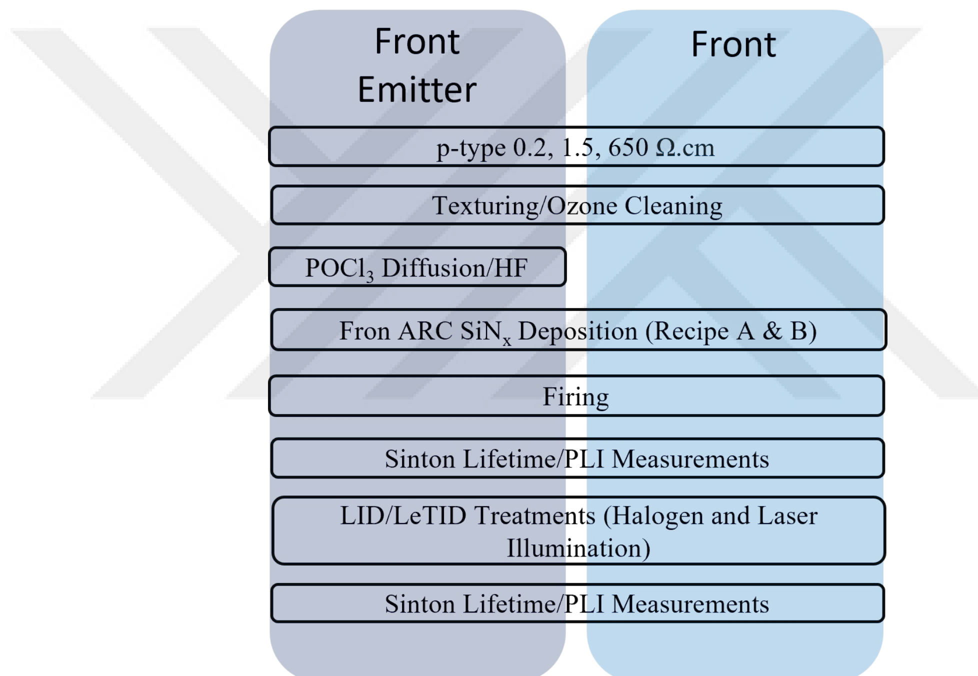

Figure 3.4: Fabrication plan of lifetime samples.

Dielectric deposition was applied for the lifetime sample fabrication sequence after the texturing and surface cleaning process. Then, samples were subjected to a firing process. The fabrication of lifetime samples is shown in *Figure 3.4*.

3.3 Investigation of LID and LeTID

3.3.1 LID Treatment

The LID mechanism, which is caused by B-O defects, was mentioned in section 2.1, according to three state model. B-O defects were at the inactive state until exposure to illumination or carrier injection and can be passivated by illuminated annealing. Within this work, illumination with halogen lamp was preferred for the degradation of samples while passivation of B-O defects was applied with two different methods: illuminated annealing with halogen lamp and hot plate, and laser illumination.

3.3.1.1 Illuminated Annealing with Halogen Lamp

For the activation of B-O defects, ~1 sun intensity illumination at ~115 °C is preferred. The level of temperature is caused by the halogen lamp itself. For the regeneration of B-O defects, the illuminated annealing process is applied. A hot plate is used as a heat source with 170 °C and ~1 sun illumination intensity. After the regeneration process, samples were followed for the stability check.

3.3.1.2 Laser Illumination

915 nm wavelength diode laser is used for the laser illumination process. For the regeneration process, samples are positioned away from the laser source to an 11.8 cm distance with 174 suns intensity and a diameter of 2.7 cm active area with 10 seconds of illumination time. No extra heat source was preferred due to the high carrier injection level of the laser and elevated heat provided itself.

3.3.2 Calculation of [Fe_i] Inside the Bulk

Due to the weak bonding strength of Fe_iB_s pairs, they can dissociate from each other during light soaking with a halogen lamp. For this purpose, samples were exposed to 1-sun intensity illumination for the fully dissociation of Fe_iB_s pairs. During the light soaking process, N_2 gas was exposed to each sample to obstruct any unwanted excess heat on samples. After the dissociation of Fe_iB_s pairs by illumination, samples were kept in a dark room well enough to let association of Fe_iB_s pairs back. Lifetime measurements were carried out after association and dissociation of those pairs.

3.3.3 Calculation of [H_{tot}] Inside the Bulk

Although there are various methods for the calculation of hydrogen atoms inside the bulk such as SIMS and DLTS, those methods can be challenging for the requirement of high vacuum or cryogenic temperatures. The variation of base resistivity of a sample by the formation of H-B bonds has been mentioned in section 2.3.3. The application of heat with a hot plate in a dark room can provide required conditions for the bonding of hydrogen and boron atoms. For this purpose, hot plate was set to 190 °C and measurements were taken hourly by Sinton WCT-120TS device.

3.3.4 LeTID Treatment

LeTID degradation occurs in a longer time when we compare it with the LID mechanism. For the investigation of LeTID, hot plate was used as heat source at 180 °C. To investigate LeTID, first, LID treatment was applied to the samples to eliminate the possible effect of B-O complexes during the LeTID degradation. Then, samples were exposed to LeTID conditions and followed.

3.4 Characterization Methods

3.4.1 Sinton WCT120TS Lifetime Tester

Effective lifetime measurement (τ_{eff}) in non-metal samples is valuable for the investigation and optimization of different layers that are used in the fabrication of a solar cell. Therefore, Sinton WCT120TS device is used for measuring the lifetime of samples. There are two main methods for determining the lifetime of a sample: quasi-steady state photoconductance decay (QSSPC) and transient photoconductance decay (PCD) methods.

In QSSPC method, a flashlight is exposed to a lifetime sample with at least 10 times slower decay constant than its lifetime, which means excess carriers are or nearly in a steady-state condition, so carrier generation and recombination are in balance [82]. Then, photoconductance in each injection level is measured by an RF coil. Due to this method, very low lifetime samples can be measured easily.

In PCD method, a short pulse of light is exposed to sample with a rapid peak and decay. Then photoconductance is measured after the evenly redistribution of carriers along the wafer. PCD method is very beneficial to measure high lifetime (>200 μs) samples.

3.4.1.1 H-B Pairs

Apart from lifetime measurements for the extraction of LID and LeTID effects, Sinton WCT120TS device also can be used for the base resistivity measurements. As mentioned in section 2.3.3, formation of H-B pairs has a certain influence on base resistivity of silicon wafer. Application of heat treatment after the firing is known to cause transfer hydrogen dimers $[H_{2A}]$ into [BH] pairs. Thus, base resistivity of the sample decreases due to hydrogen passivation of dopant atoms. By using measured resistivities after heat application, absolute hydrogen concentration can be

calculated. For the annealing, 190 °C was preferred in a dark room. By measuring samples at a certain time interval, base resistivity variations were followed.

3.4.2 Sinton SunsV_{oc} Tester

The measured V_{oc} value of a cell is an important parameter in investigating cell quality and variations on it. By using Sinton SunsV_{oc} tester, investigation on a cell can be done easily and rapidly. During the measurement of V_{oc} value, the illumination intensity that is exposed to the sample is critical. For the measurement, contacts from the front and rear sides must be taken.

3.4.3 Sun I-V Sorter

Sun I-V sorter device is a measurement method for solar cells. It takes contacts by probes according to the same number with busbar and multiple pins on each probe. By homogeneously contacting along the cell from metallized regions, V_{oc}, J_{sc}, FF and η measurements can be done successfully.

CHAPTER 4

RESULTS AND DISCUSSION

Sample fabrication was divided into two main groups: cell and lifetime groups. In the lifetime group, samples were fabricated symmetrically. To investigate the effect of the front passvation layer, two different recipes for the silicon nitride layer, SiNA and SiNB, were preferred, and they deposited to textured wafers with base resistivities of 0.2, 1.5, 650 Ω.cm. In addition, as symmetrical lifetime group of samples with emitter was fabricated. After the texturing process, samples underwent a diffusion process to form an emitter at both sides of the wafer. Then, the same passivation group of SiNA and SiNB was deposited separately on three different base resistivity samples. Finally, the fabrication of cell samples was carried out. Rear passivation layer was kept identical for all samples group. While, for the front passivation layer, SiNA and SiNB were preferred in identical samples to compare front side passivation layer effects on the solar cell. Lifetime samples were cut into 5 cm x 5cm samples with a marker laser. For the investigation of lifetime samples, three different small samples from identical wafers which was preferred identical positions from the wafer used.

4.1 Fabricated Samples

Fabricated samples with their labels were identified in the table below. Base resistivities of 0.2, 1.5, and 650 Ω.cm samples were used as substrates. Emitter formation was applied to Groups A, B, E, F, J and K symmetrically for lifetime samples and one-sided for cell samples. While in samples of Group C, D, G, H, L and M, emitter formation was not preferred and only lifetime samples were fabricated from those samples.

Table 4.1: *Labels of fabricated samples*.

0.2 Ω.cm				1.5 Ω.cm				650 Ω.cm			
With emitter		Without emitter		With emitter		Without emitter		With emitter		Without emitter	
SiNA	SiNB	SiNA	SiNB	SiNA	SiNB	SiNA	SiNB	SiNA	SiNB	SiNA	SiNB
Group A	Group B	Group C	Group D	Group E	Group F	Group G	Group H	Group J	Group K	Group L	Group M

To understand the characteristics of the passivation layers of SiNA and SiNB, the simulation results of J_{Gen} and losses due to the reflection and absorption was shown in the table below.

Table 4.2: *The simulation results of J_{Gen} and losses caused by reflection and absorption for SiNA and SiNB* [85].

Name of Recipe	Refractive Index	Loss in J_{Gen} (mA.cm^{-2})		J_{Gen} (mA.cm^{-2})
		Reflection	Absorption	
SiNA	2.18	0.48	0.36	43.60
SiNB	2.04	0.64	0.01	43.79

According to the table Table 4.2, J_{Gen} was higher for SiNB passivation layer. Although the loss in reflection was higher in SiNB, it had almost zero absorption. On the other hand, SiNA has a certain loss because of both reflection and absorption.

After the fabrication of cell samples, they were measured with Sun I-V Sorter. According to the results in Table 4.3, SiNB samples of Group B, F and K had higher η_{eff} and J_{sc} values than SiNA samples of Group A, E and J. The difference in initial measurement of fabricated cells can be explained by Table 4.2. The difference in losses on J_{Gen} caused by the reflection and absorption from the passivation layer at the front directly affected the J_{sc} and caused a difference in cell efficiency.

Table 4.3: *The average results of fabricated cell samples.*

	$J_{sc,average}$	$\eta_{eff,average}$
Group A	37.6	19.6
Group B	38.0	19.8
Group E	38.6	20.0
Group F	39.0	20.1
Group J	35.7	17.0
Group K	35.9	17.3

The results of lifetime samples as shown below. The highest lifetime values were observed in 650 Ω.cm base resistivity samples of Group J, K, L and M. The reason was the lack of dopant concentration causes low recombination which means higher lifetime for generated electron-hole pairs.

Table 4.4: *Sinton WCT-120TS measurement results of lifetime samples.*

Samples	$T_{eff,average}$	$iV_{oc,average}$
Group A	8.0	646
Group B	8.2	648
Group C	11	654
Group D	14	660
Group E	65	654
Group F	71	656
Group G	107	668
Group H	122	672
Group J	515	653
Group K	540	654
Group L	1250	670
Group M	1370	673

For 0.2 Ω.cm base resistivity samples of Group A, B, C and D, lifetime values were the lowest because of excess concentration of dopant atoms that caused higher recombination for generated electron-hole pairs.

4.2 Investigation of LID

To investigate LID mechanism, degradation and regeneration processes were optimized separately. The optimization of recipes was carried on lifetime samples first, then applied to cell samples.

4.2.1 Optimization of Degradation Process

Light soaking (LS) under 1-sun intensity with a temperature of ~115 °C was applied to investigate LID degradation. The heat source during the light soaking step was the halogen lamp itself, and no extra heat was applied apart from it. The response of samples under light soaking conditions was shown in the figure below.

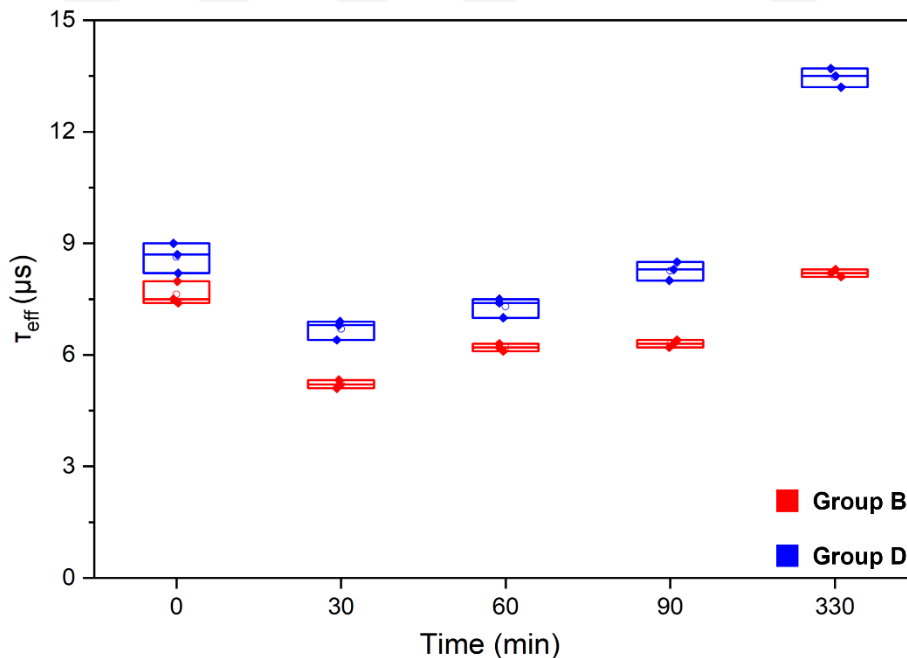

Figure 4.1: Degradation with light soaking of identically passivated 0.2 Ω.cm base resistivity samples with emitter, Group B and without emitter, Group D samples.

According to *Figure 4.1*, in 30 minutes, 0.2 Ω.cm base resistivity samples were degraded and no further degradation occurred for a longer duration of exposure. Instead, as the exposure time increased, a recovery was observed in samples. To check the stability of that recovery, samples were kept in a dark room for some time. Measurements were carried out once and τ_{eff} values were dropped approximately to the initial values of samples.

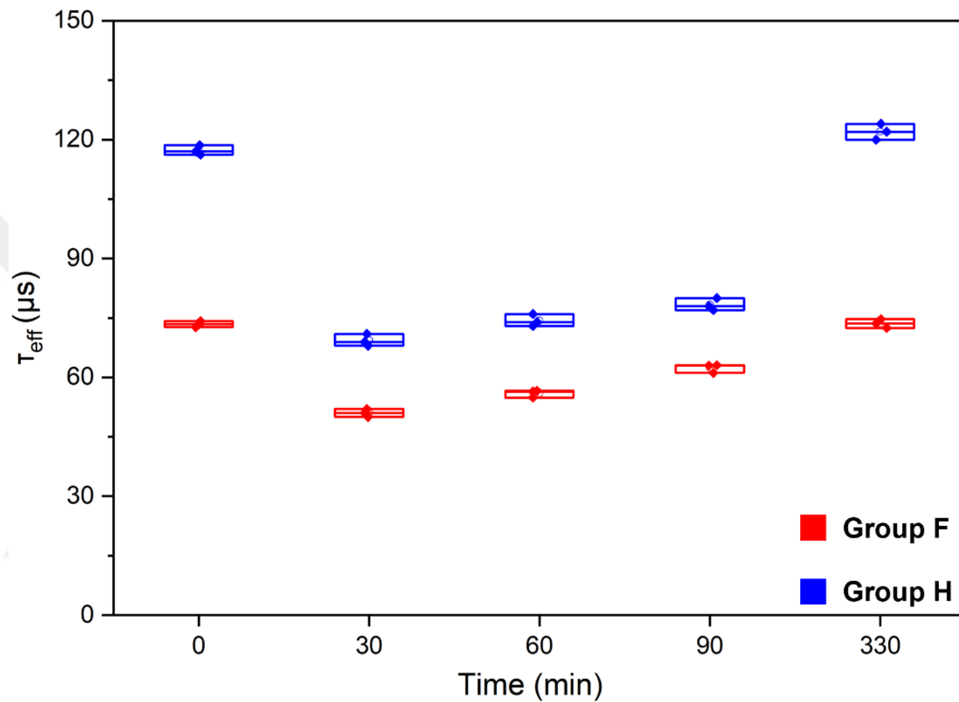

Figure 4.2: Degradation with light soaking of identically passivated 1.5 Ω.cm samples with emitter, Group F and without emitter, Group H samples.

As depicted in *Figure 4.2*, the degradation process response of Group F and H were in the same trend as Group B and D. From the measured results of samples after some time, they were recovered to their initial value as in Group B and Group D.

The results of 650 Ω.cm base resistivity samples with the application of light soaking for the degradation was shown in the figure below. Although Group M samples showed an increase in τ_{eff} after 30 minutes of light soaking, Group K showed slight or no change to light soaking process. Due to the very low boron dopant concentration level at the bulk, the formed concentration of B-O defects on both

Group K and M was very low. Therefore, a small or no change was expected in τ_{eff}. To understand the origin of the increase in Group K samples, equivalent samples were subjected to heat treatment which was identical to the heat of the samples that were exposed during the light soaking for 30 minutes. According to the τ_{eff} and J_0 results, there was no significant change was observed due to the heat treatment. Therefore, the increase in τ_{eff} can be attributed to the carrier injection effect of the light soaking process.

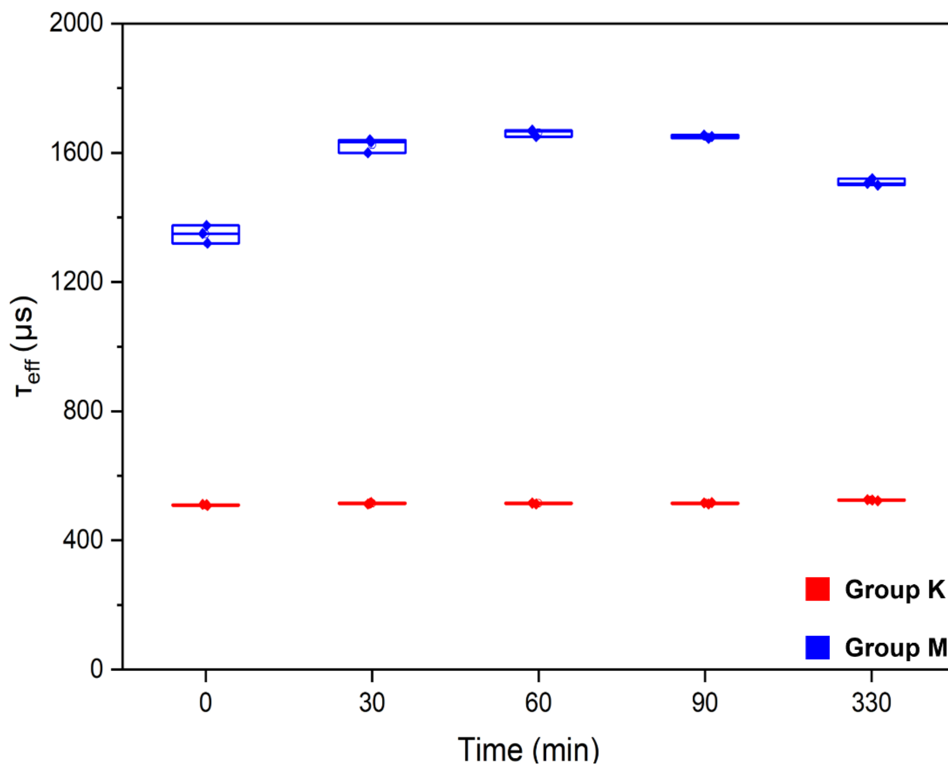

Figure 4.3: Degradation with light soaking response of identically passivated 650 Ω.cm samples with emitter, Group K and without emitter, Group M samples.

However, when we compared the surface recombination (J_0) values at initial and after 30 minutes of light soaking, for Group M samples, a reduction in J_0 was observed while there was no change in J_0 of Group K samples. In other words, 30 minutes of light soaking can reduce the J_0 in the absence of an emitter while it can be increased again with a longer duration of light soaking application.

4.2.2 Dark Annealing Enhanced Degradation Process

Dark annealing is known for its ability to recover B-O related degradation mechanism temporarily. One more critical effect of dark annealing is providing inactive defects from precursor State D to State A as mentioned in section 2.1. For the investigation of State D as depicted in three state model, samples were exposed to a dark annealing process at 200 ℃ after the light soaking step. Then, they were exposed to further light soaking steps to observe increased degradations.

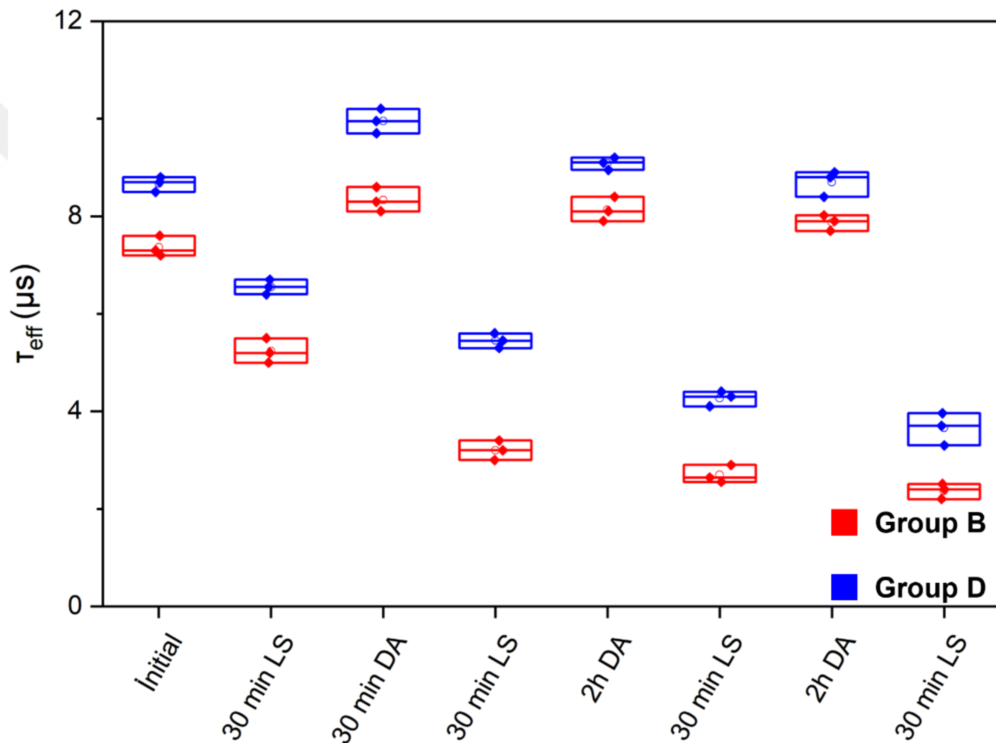

Figure 4.4: Dark annealing enhanced degradation of identically passivated 0.2 Ω.cm samples with emitter, Group B and without emitter, Group D samples at 200 ℃.

As in the figure above, the degradation extent after the first and second light soaking process was increased after dark annealing in both Group B and D samples. B-O defects concentration in State A was increased with dark annealing application which was expected [13], [86]. Therefore, a dark annealing process was required for higher extent of B-O defects passivation.

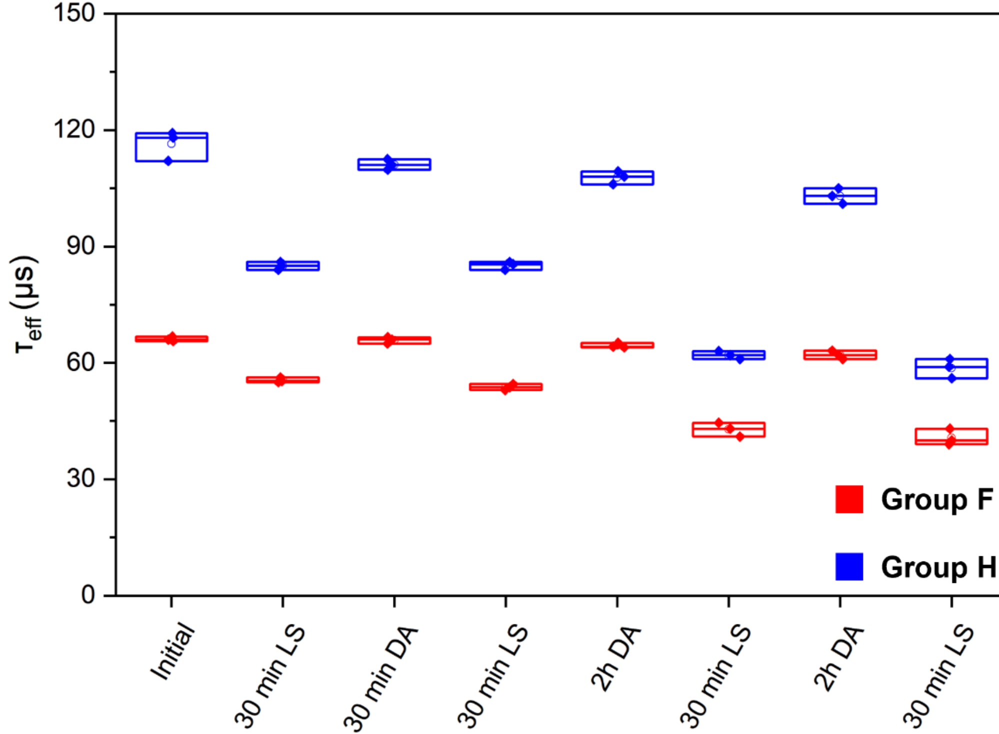

Figure 4.5: Dark annealing enhanced degradation of identically passivated 1.5 Ω.cm samples with emitter Group F and without emitter, Group H samples at 200 °C.

Also, the same phenomenon, increased activation of B-O defects by dark annealing application was observed in the samples of Group F and H. Therefore, integrating the dark annealing step for the permanent passivation of B-O LID can be beneficial for an advanced level of regeneration and stability of samples. However, the duration and temperature of dark annealing application should be decided carefully. According to the time and temperature of the application, it can cause whether enhancement or reduction of degradation caused by LeTID mechanism [53].

Normalized defect density (N_{BO}^{*}) of B-O defects can be used to investigate the effect of dark annealing on the concentration of B-O complex. As described in section 2.1.1, Eq. (2.1) was used for calculations.

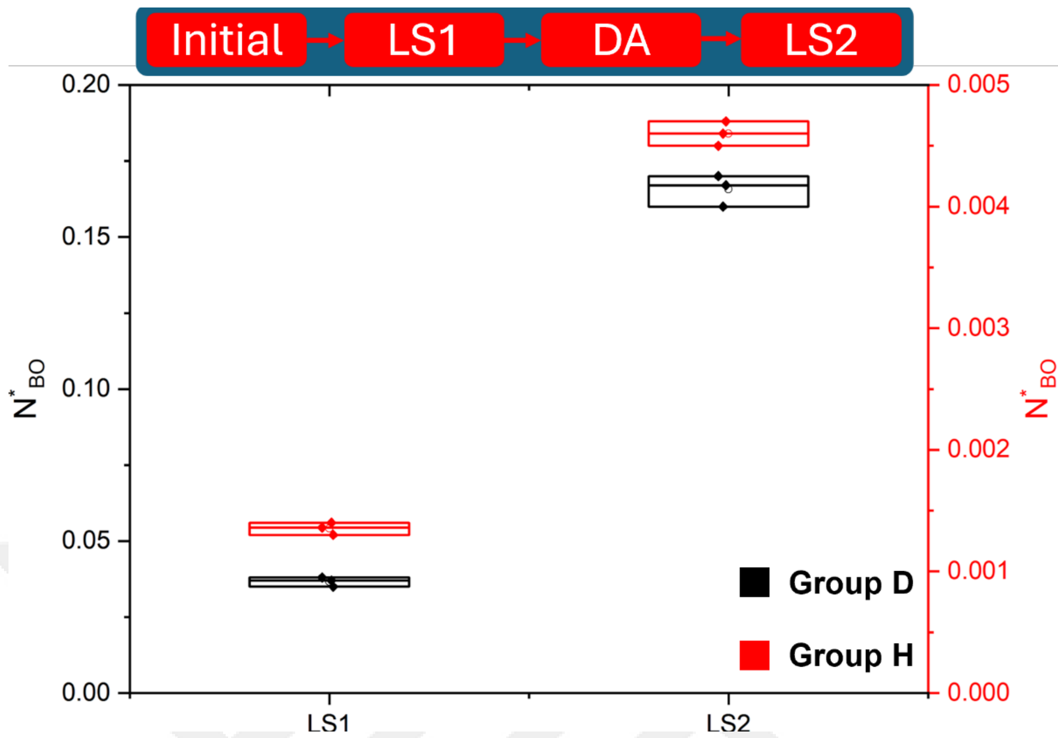

Figure 4.6: Normalized defect density of B-O defects for identically passivated Group D with 0.2 Ω.cm base resistivity and Group H with 1.5 Ω.cm base resistivity. LS1 is degradation after the initial condition while LS2 is degradation after dark annealing application, dashed lines are guide to eyes.

Group D and H samples were exposed to LS1 with 30 minutes of illumination under 1-sun intensity. Then, they were exposed to a dark annealing step for temporary recovery from a degraded state. After applying LS2 following the dark annealing, there was a certain increase in N^*_{BO} triggered by dark annealing that supplied B-O defects to State A from State D [86]. Moreover, the concentration of N^*_{BO} of 0.2 Ω.cm base resistivity samples was significantly higher than 1.5 Ω.cm samples as expected [20]–[22].

4.2.3 Optimization of Regeneration Process

After the degradation process of B-O defects, they need to undergo a regeneration process to recover from the degraded state. The regeneration process, which also can be called hydrogenation, with a halogen lamp and heat application by a hot plate was

investigated for the recovery. The effect of different temperature of hot plate was investigated by keeping the one sun intensity value constant.

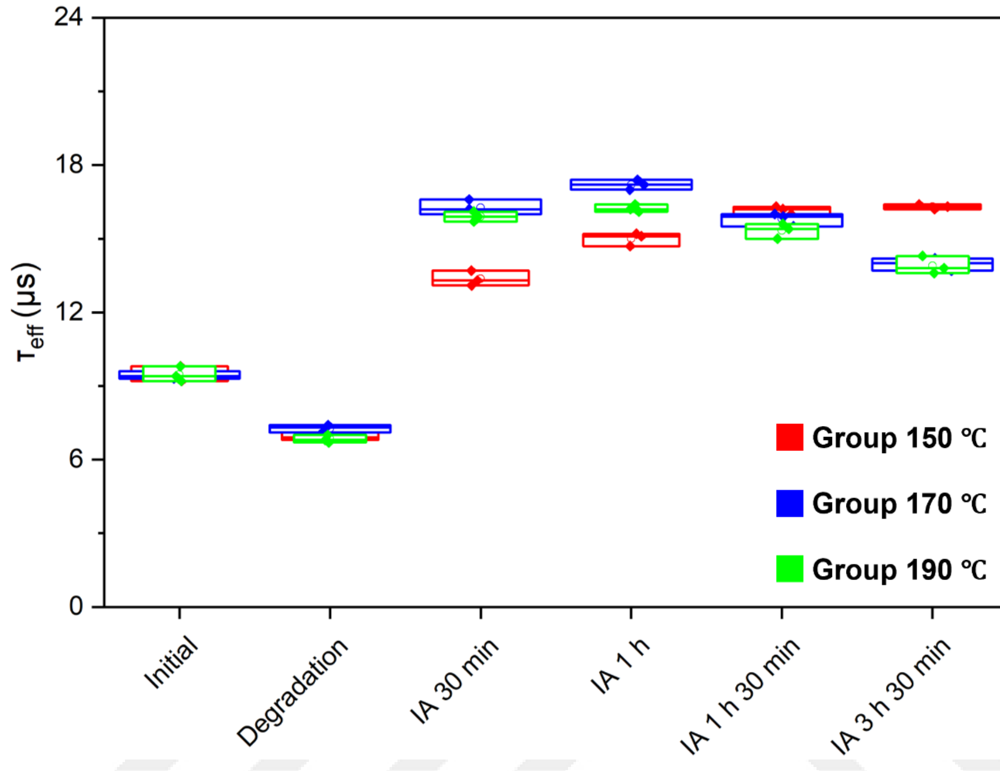

Figure 4.7: Optimization of B-O LID regeneration process on 0.2 Ω.cm samples of Group D with a constant illumination of 1-sun intensity and varying temperatures of 150, 170 and 190 °C.

As in *Figure 4.7*, during the 150 °C illuminated annealing, effective lifetime increases as the duration of exposure. However, regeneration was not permanent in further measurements after some time. Thus, 150 °C only recovers degraded lifetime temporarily. Also, the change during 190 °C treatment was not as significant as 170 °C and caused further degradation of samples after a while. On the other hand, at 170 °C, the regeneration was maximum and permanent at 1 hour treatment for 0.2 Ω.cm base resistivity.

According to *Figure 4.8*, 170 °C temperature with one sun intensity illumination for 30 minutes seems the best recipe for 1.5 Ω.cm base resistivity samples. Although samples showed a recovery under illuminated annealing at 150 °C temperature, it

was not stable. After some time, the lifetime value dropped significantly. On the other hand, a degradation from the regenerated state was observed after some time on 190 °C illuminated annealing samples. Thus, the regeneration recipe for B-O LID should be adjusted according to the base resistivity of the samples due to different concentrations of B-O defects.

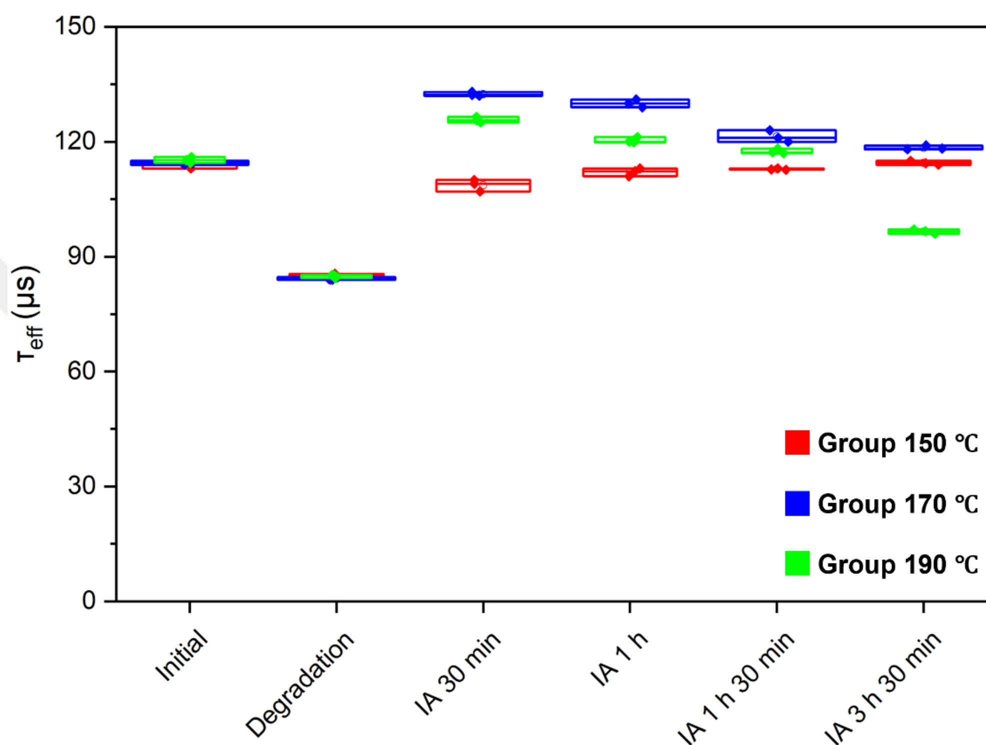

Figure 4.8: Optimization of B-O LID regeneration process on 1.5 Ω.cm samples of Group H with a constant illumination of 1-sun.

After optimizing LID cycle on lifetime samples, the optimized recipes were applied to cell samples of Groups A, B, E, and F. According to the results, diffused hydrogen inside the bulk from both passivation layers of SiNA and SiNB was enough to passivate B-O defects successfully. Therefore, no difference in B-O LID regeneration was observed on differently passivated samples. On the other hand, a significant difference in ΔV_{oc} in base resistivity of 0.2 and 1.5 Ω.cm base resistivity samples was observed as expected [20]–[22]. As the concentration of boron dopant atoms increased, the extent of B-O related degradation also increased.

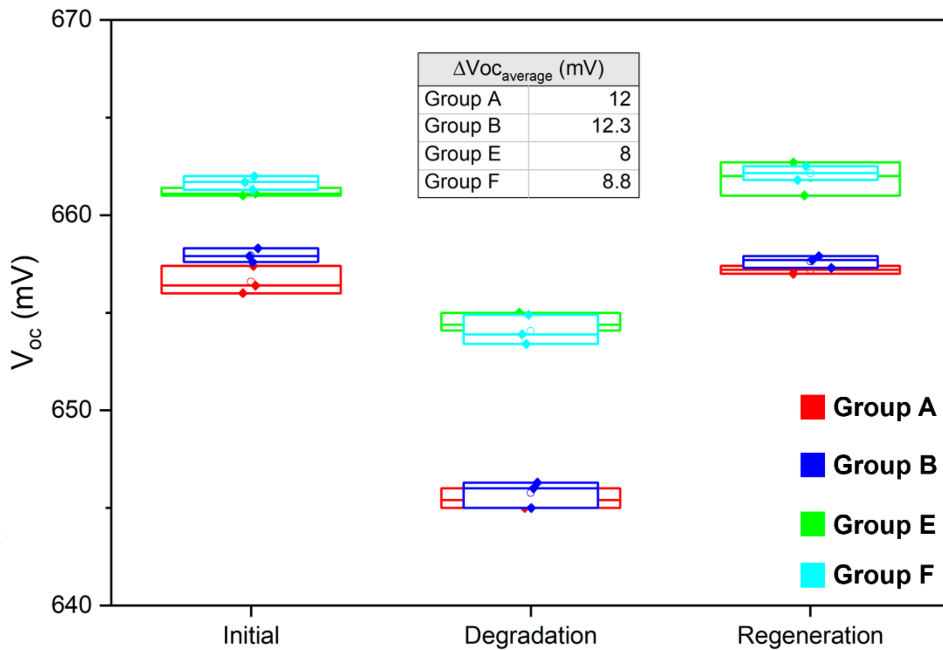

Figure 4.9: Regeneration of cell samples of 0.2 Ω.cm base resistivity Group A and B passivated with SiNA and SiNB, and 1.5 Ω.cm base resistivity Group E and F passivated with SiNA and SiNB.

To investigate the effect of dark annealing application on the degradation and stability, the best recipe for B-O regeneration with 170 °C with one sun intensity was applied to 1.5 Ω.cm samples of Group G, with SiNA passivation and Group H, with SiNB passivation. According to the results of each LID cycle as in *Figure 4.10*, they were close to each other among the same nitride groups as expected until the stability check step. Group G and H samples showed a certain degradation after regeneration of B-O defects. However, the same group of samples except those exposed to dark annealing did not show degradation yet. The reason was the effect of dark annealing on supplying inactive defects from precursor State D to State A. Providing those defects into State A can be activated during the second light soaking step. In other words, the extent of degradation from B-O defects was increased. Finally, by applying illuminated annealing, more B-O defects were passivated and the stability of the samples was enhanced. Without dark annealing application, State D can supply B-O defect into State A during increased heat conditions in the future. Therefore, the sample will have a higher potential to degrade under sunlight.

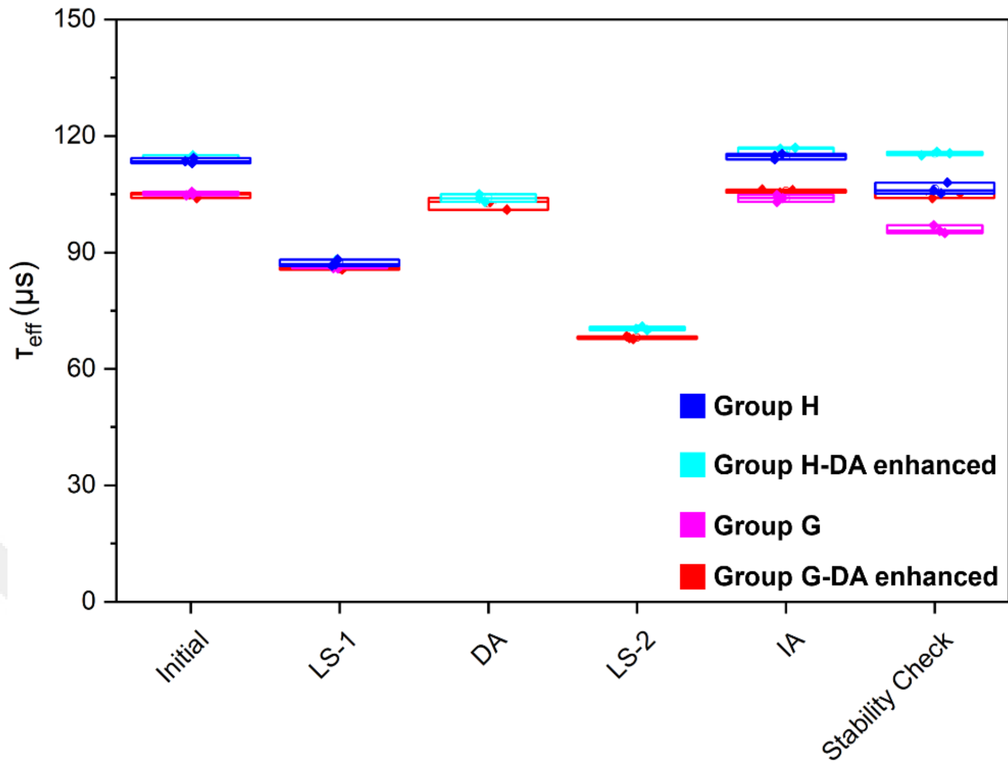

Figure 4.10: The effect of dark annealing enhanced B-O defect activation on LID regeneration on 1.5 Ω.cm samples of Group G with passivation of SiNA and Group H with passivation SiNB.

For the regeneration, as an alternative way to a halogen lamp and hot plate method, a 915 nm diode laser was used for the first time. As indicated in section 2.1.2, laser hydrogenation provides fast and advanced passivation for existing defects. For this purpose, samples were degraded first, to observe the regeneration B-O defects of the laser. Then, 124 ± 5 suns intensity for 10 seconds was applied to samples for the regeneration. According to the results in *Figure 4.11*, both samples with 0.2 Ω.cm base resistivity responded to hydrogenation. The results after laser hydrogenation were stable. However, their τ_{eff} after regeneration was not as high as halogen lamp and hot plate method that were applied to identical samples of same groups. One of the reasons can be the duration of time. Although 10 seconds was enough to passivate a certain amount of B-O defects, a longer period may be needed to passivate more defects for 0.2 Ω.cm base resistivity samples.

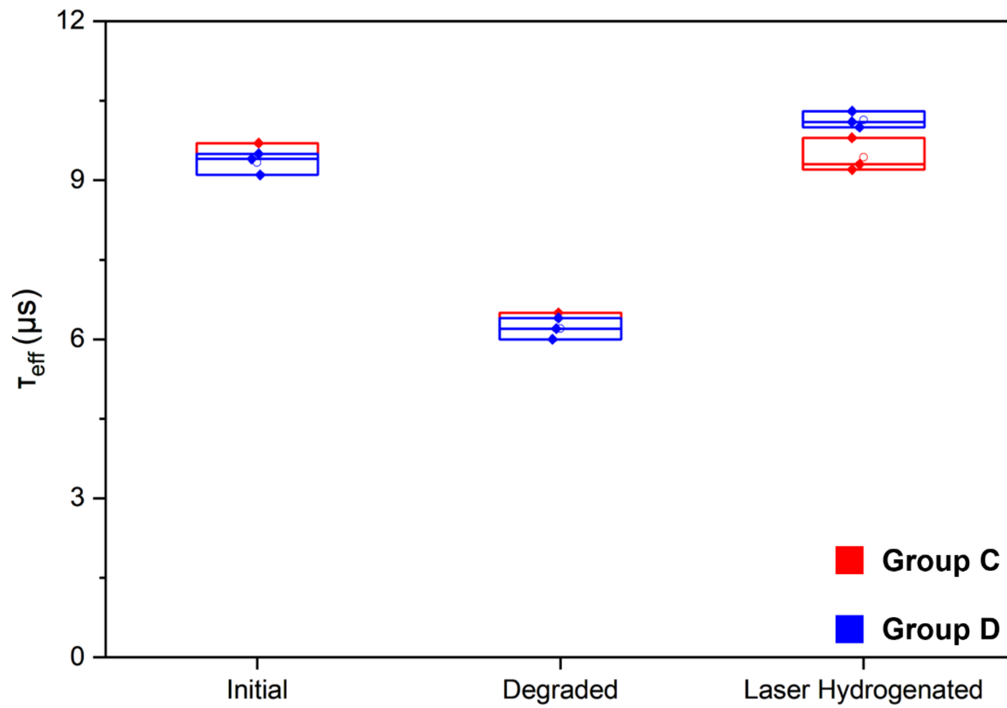

Figure 4.11: The results of laser hydrogenation with 915 nm diode laser under 124 ± 5 suns intensity of 0.2 Ω.cm base resistivity samples of Group C and D passivated with SiNA and SiNB.

In *Figure 4.12*, laser hydrogenation of 1.5 Ω.cm base resistivity group of samples was applied to Group G, passivated with SiNA and Group H, passivated with SiNB samples. According to the results, 10 seconds was enough to passivate B-O complex at the same rate as halogen lamp and hot plate method and the results were stable. τ_{eff} results of identical samples that regenerated with two different methods were at the same level. In other words, laser hydrogenation with 915 nm diode laser can be used as a fast and effective way for the hydrogenation of B-O defects.

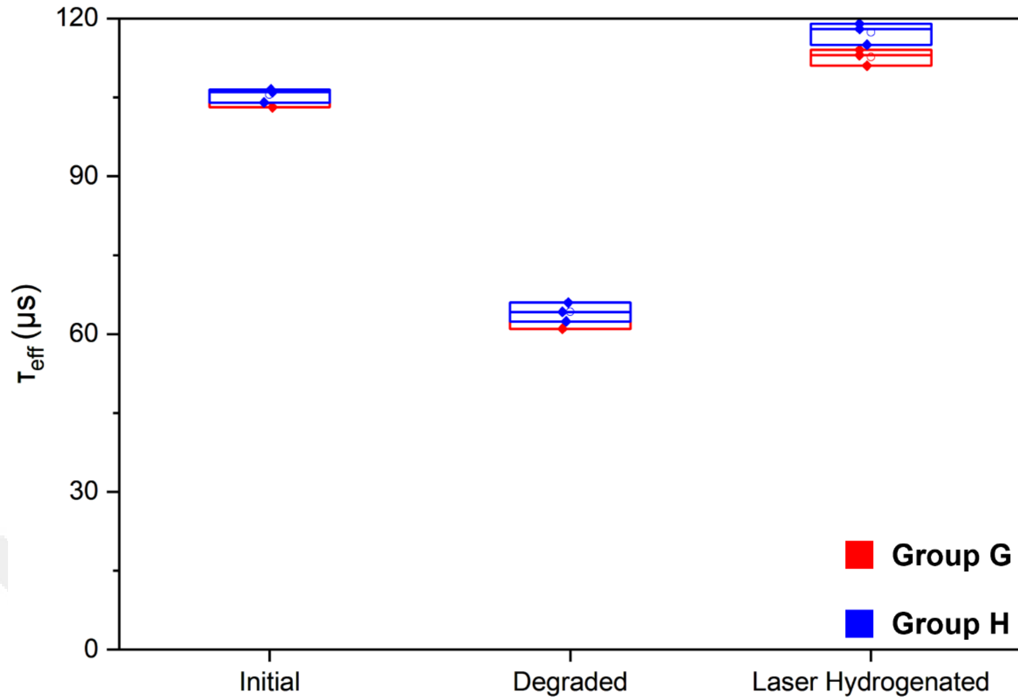

Figure 4.12: The results of laser hydrogenation with 915 nm diode laser under 124 ± 5 suns intensity of 1.5 Ω.cm base resistivity samples of Group G and H passivated with SiNA and SiNB.

4.2.4 Determination of Diffused Hydrogen Concentration Inside the Bulk

For the calculation of hydrogen concentration inside the bulk, the variations in base resistivity of the samples were followed. For this experiment, base resistivity variation on 1.5 Ω.cm base resistivity samples was followed. 650 Ω.cm base resistivity could not be used because the maximum base resistivity that Sinton WCT-120TS device can measure is 100 Ω.cm. On the other hand, in 0.2 Ω.cm samples, the dopant concentration was too high. In other words, too many boron atoms can form bonds with hydrogen atoms. However, as the dopant concentration increases, the change in base resistivity with a constant hydrogen concentration inside the bulk that bonds with boron atoms becomes undetectable. Therefore, base resistivity observation on 0.2 Ω.cm samples was challenging. The variations in base resistivity of the 1.5 Ω.cm samples under dark annealing at 190 °C for 9 hours were shown in *Figure 4.13*. Although the initial base resistivities of SiNA and SiNB passivated

samples were identical, their response to dark annealing which was known to cause the formation of B-H pairs were different. The amount of H-B pairs formed was higher in SiNB samples deduced from the base resistivity variation. As the base resistivity of the sample increases, it means more boron dopant atoms formed bonding with hydrogen atoms. Therefore, the concentration of hydrogen diffused into the bulk was higher in SiNB passivated samples than in SiNA passivated samples.

The refractive index of SiNA was 2.18 and SiNB was 2.04. SiNA had a less dense structure and higher hydrogen concentration than SiNB. However, hydrogen atoms are more prone to exist in H_2 form in less denser structures. Moreover, H_2 form of hydrogen atoms was more prone to effuse environment instead of diffusing inside the bulk during the firing [71]. On the other hand, in SiNB, hydrogen atoms was in a monoatomic state. Therefore, the diffusion of hydrogen atoms inside the bulk was easier and the higher hydrogen concentration diffused to the bulk in SiNB passivated samples as expected [61].

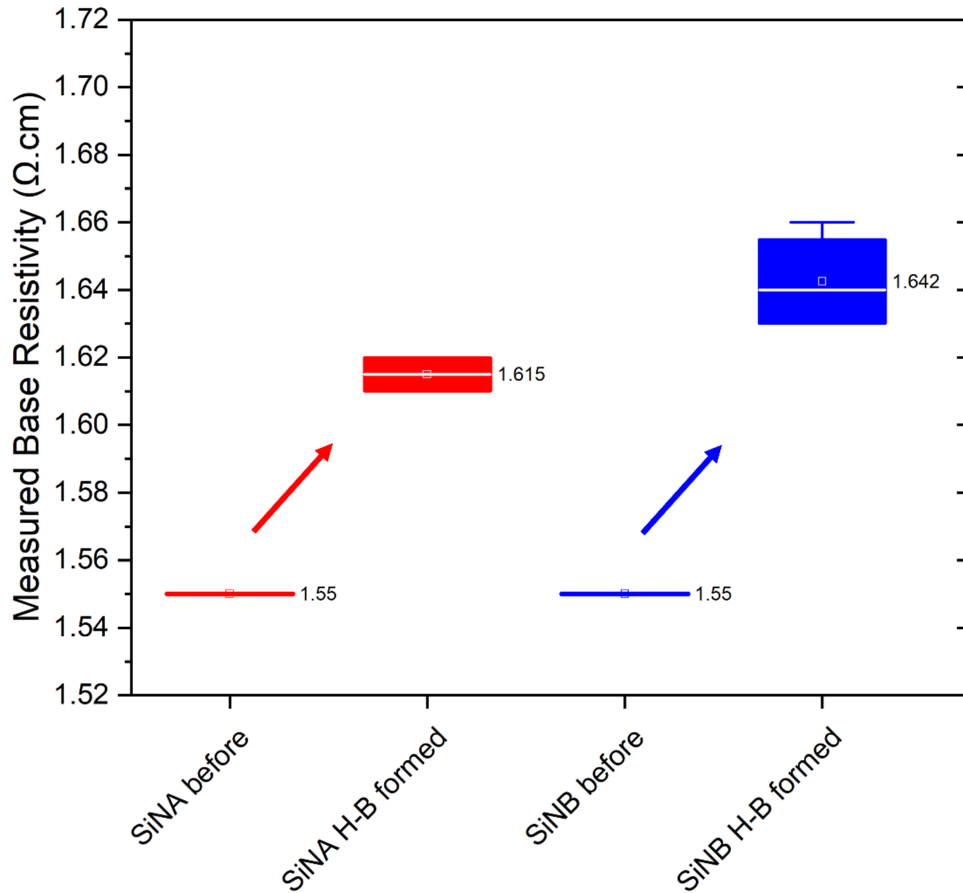

Figure 4.13: The average variation of base resistivity on 1.5 Ω.cm base resistivity samples symmetrically passivated with SiNA and SiNB by dark annealing at 190 °C for 9 hours.

To calculate the diffused hydrogen concentration into the bulk, Eq. (2.12-18) was used. The calculated results are as in the table below.

Table 4.5: *Calculated hydrogen concentrations of deposited silicon nitride layers.*

Silicon Nitride Layer	Hydrogen Concentration (cm^{-3})
SiNA	7.75×10^{14}
SiNB	1.00×10^{15}

The concentration of hydrogen atoms in the bulk was higher in samples passivated with SiNB layer 2.25×10^{14} cm^{-3} than in SiNA layer passivated samples.

4.2.5 Calculation of Iron Impurities

For the investigation of iron concentration inside the bulk, measurements after the association and dissociation of Fe_iB_s pairs with light soaking and dark room storage were followed [46]. The critical point for determining time requirement for the light soaking for fully dissociation, lifetime value can be followed. Due to the asymmetric capture cross-section of iron impurities, the lifetime value increases with the dissociation of pairs [45]. To determine the illumination durations for the fully dissociation of Fe_iB_s, they were exposed to halogen lamp illumination for short time scales. Illumination was set to 1-sun intensity. During the illumination, to obstruct the possibility of excess heat of more than 50 °C, N_2 gas was exposed to the samples to prevent any change in base resistivity.

Table 4.6: *Required times for association and dissociation of Fe_iB_s pairs for 0.2, 1.5 and 650 Ω.cm base resistivity groups.*

Dopant Concentration N_A (cm^{-3})	Base Resistivity (Ω.cm)	Required time for the dissociation of Fe_iB_s pairs	Time needed for the formation of 5% Fe_iB_s pairs	Required time for the formation of 95% Fe_iB_s pairs
9.7×10^{15}	1.5	70 sec	80 sec	1.2 h
1×10^{17}	0.2	30 sec	7 sec	7 min

The optimized time requirements for the complete dissociation of Fe_iB_s pairs was as shown in the table above. Also, from Eq. (2.2-3), the required time for the association of Fe_iB_s pairs for each base resistivity group of 0.2 and 1.5 Ω.cm was calculated as shown in Table 4.6. To calculate the constant C, v_{th} was taken 1.1 x 10^{17} cm/s [87], while $\sigma_n^{Fe_i}$, $\sigma_p^{Fe_i}$, σ_n^{FeB} and σ_p^{FeB} was taken from [88]. The lifetime measurements were done at varied excess minority carrier density (Δn) values according to the base resistivities of samples [45]. After waiting well enough to let fully association of

Fe_iB_s pairs, iron concentrations of each ingot group were calculated using Eq. (2.4) from the measured lifetime results.

Table 4.7: *The concentration of Fe_i impurities at each ingot.*

Base Resistivity (Ω.cm)	**Iron concentrations (cm^3)**	**Measured loss in pseudo efficiency ($\%_{abs}$) caused by iron contamination**
1.5	$(1.8 \pm 0.2) \times 10^{11}$	0.1
0.2	$(3.8 \pm 0.4) \times 10^{11}$	0.2

The iron concentration of each ingot group as shown in Table 4.7. The results are compatible with the literature [89]. Also, loss in pseudo efficiency caused by iron contamination was measured.

4.3 Investigation of LeTID

For the investigation of LeTID, boron-doped samples were exposed to LID regeneration process to prevent any B-O defect related effects interference during LeTID investigation. Following the regeneration process, samples were exposed to LeTID condition which is 180 °C set temperature with a hot plate for 40,000 minutes. According to the results, both samples showed LeTID related degradation at a certain level. Although the hydrogen concentration inside the bulk of Group H samples was 2.25×10^{14} cm^{-3} higher than that of Group G samples, the levels that they degraded were very close to each other. However, Group H showed a faster degradation than Group G samples in contrast to literature [59].

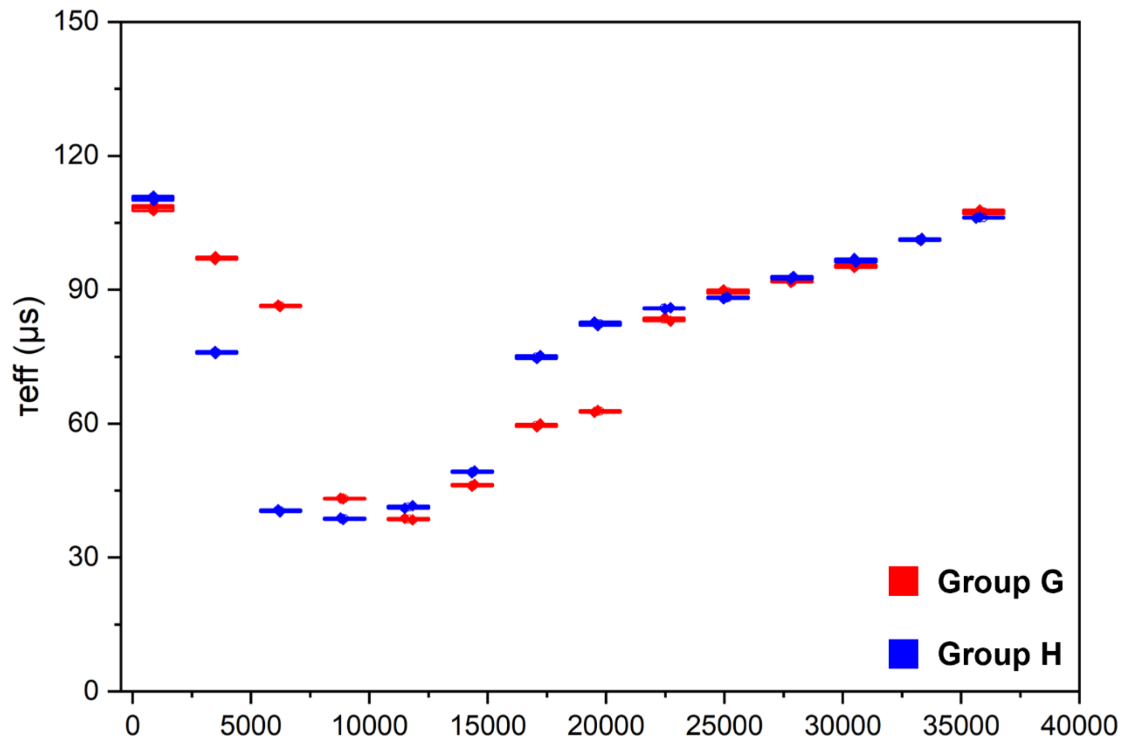

Figure 4.14: LeTID response of Group G and Group H samples at 180 °C heat in a dark room.

Thus, a higher hydrogen concentration in the bulk caused a faster LeTID while lower hydrogen concentration required a longer time for fully degradation and recovery. On the other hand, 2.25 x 10^{14} cm^{-3} difference in hydrogen concentration did not affect the extent of LeTID at a significant rate.

CHAPTER 5

CONCLUSION

In this thesis, the effect of base resistivity and varying hydrogen concentrated silicon nitride passivation layers on the B-O LID and LetTID mechanisms was investigated. According to the results, base resistivity significantly impacts the extent of B-O degradation. By calculating N^*_{BO} values of 0.2 and 1.5 Ω.cm base resistivity samples, the dependence of B-O defect concentration on base resistivity was investigated. N^*_{BO} of 0.2 Ω.cm samples was calculated higher than 1.5 Ω.cm base resistivity samples. On the other hand, the concentration of diffused hydrogen into the bulk from both layers was observed sufficiently enough to passivate B-O defects fully. In addition, the effect of the thermal precursor state of B-O defects State D was observed by applying a light soaking following the dark annealing. An increased degradation compared to first light soaking process was a proof of the existence of State D for B-O defects.

To calculate hydrogen concentration inside the bulk, samples were exposed to a temperature of 190 °C on a hot plate in a dark room. By measuring the base resistivity of samples hourly, base resistivity variation was followed. Hydrogen concentration inside bulk on samples was calculated from base resistivity variations.

Laser hydrogenation as an alternative method for the regeneration of B-O complex was performed with a 915 nm diode laser with 124 ± 5 suns intensity for 10 seconds. According to results, a fast and stable regeneration method was successfully performed.

To calculate iron concentration in each group of samples, they were exposed to a short light soaking under 1-sun illumination with a cooling condition. Iron

concentrations were calculated by measuring effective lifetime values after light soaking and dark storage.

To investigate LeTID mechanism, samples were exposed to a B-O passivation step to obstruct any interference with LID. Then, samples were placed on a hot plate with a 180 °C set temperature. Measurements were carried out periodically to observe variations related to LeTID. According to the results, the extent of degradation caused by LeTID was the same for hydrogen-concentrated samples. However, as the hydrogen concentration increases, degradation occurs faster than in lower hydrogen concentrated samples. In other words, increasing hydrogen concentration caused a faster degradation.

Thus, base resistivity directly affects the extent of B-O related degradation. Although diffused hydrogen concentration into the bulk was different on SiNA and SiNB passivated samples, it was enough for the passivation of B-O defects in both group of samples. Finally, increased hydrogen concentration caused a faster formation of LeTID instead of causing higher extent of degradation.

REFERENCES

[1] R. Singh, “Why silicon is and will remain the dominant photovoltaic material,” *J Nanophotonics*, vol. 3, no. 1, 2009, doi: 10.1117/1.3196882.

[2] A. W. Blakers, A. Wang, A. M. Milne, J. Zhao, and M. A. Green, “22.8% efficient silicon solar cell,” *Appl Phys Lett*, vol. 55, no. 13, 1989, doi: 10.1063/1.101596.

[3] C. Zhang, J. Zhang, Y. Hao, Z. Lin, and C. Zhu, “A simple and efficient solar cell parameter extraction method from a single current-voltage curve,” *J Appl Phys*, vol. 110, no. 6, 2011, doi: 10.1063/1.3632971.

[4] F. A. Lindholm, J. G. Fossum, and E. L. Burgess, “Application of the Superposition Principle to Solar-Cell Analysis,” *IEEE Trans Electron Devices*, vol. 26, no. 3, 1979, doi: 10.1109/T-ED.1979.19400.

[5] A. D. Dhass, E. Natarajan, and L. Ponnusamy, “Influence of shunt resistance on the performance of solar photovoltaic cell,” in *Proceedings - ICETEEEM 2012, International Conference on Emerging Trends in Electrical Engineering and Energy Management*, 2012. doi: 10.1109/ICETEEEM.2012.6494522.

[6] S. Bowden and A. Rohatgi, “RAPID AND ACCURATE DETERMINATION OF SERIES RESISTANCE AND FILL FACTOR LOSSES IN INDUSTRIAL SILICON and SOLAR CELLS,” in *17th European Photovoltaic Solar Energy Conference*, 2001.

[7] A. Richter, S. W. Glunz, F. Werner, J. Schmidt, and A. Cuevas, “Improved quantitative description of Auger recombination in crystalline silicon,” *Phys Rev B Condens Matter Mater Phys*, vol. 86, no. 16, 2012, doi: 10.1103/PhysRevB.86.165202.

[8] P. P. Altermatt, J. Schmidt, G. Heiser, and A. G. Aberle, "Assessment and parameterisation of Coulomb-enhanced Auger recombination coefficients in lowly injected crystalline silicon," *J Appl Phys*, vol. 82, no. 10, 1997, doi: 10.1063/1.366360.

[9] E. Yablonovitch and T. Gmitter, "Auger recombination in silicon at low carrier densities," *Appl Phys Lett*, vol. 49, no. 10, 1986, doi: 10.1063/1.97049.

[10] H. Savin, G. Kissinger, and V. M. Airaksinen, "Measuring oxygen and bulk microdefects in silicon," in *Handbook of Silicon Based MEMS Materials and Technologies*, 2020. doi: 10.1016/B978-0-12-817786-0.00037-2.

[11] A. Herguth, G. Schubert, M. Kaes, and G. Hahn, "A new approach to prevent the negative impact of the metastable defect in boron doped CZ silicon solar cells," in *Conference Record of the 2006 IEEE 4th World Conference on Photovoltaic Energy Conversion, WCPEC-4*, 2006. doi: 10.1109/WCPEC.2006.279611.

[12] V. P. Markevich *et al.*, "Boron–Oxygen Complex Responsible for Light-Induced Degradation in Silicon Photovoltaic Cells: A New Insight into the Problem," *Physica Status Solidi (A) Applications and Materials Science*, vol. 216, no. 17, 2019, doi: 10.1002/pssa.201900315.

[13] B. Hallam *et al.*, "Eliminating light-induced degradation in commercial p-Type Czochralski silicon solar cells," *Applied Sciences (Switzerland)*, vol. 8, no. 1. 2017. doi: 10.3390/app8010010.

[14] S. W. Glunz, S. Rein, W. Warta, J. Knobloch, and W. Wettling, "Degradation of carrier lifetime in Cz silicon solar cells," *Solar Energy Materials and Solar Cells*, vol. 65, no. 1, 2001, doi: 10.1016/S0927-0248(00)00098-2.

[15] D. C. Walter, B. Lim, K. Bothe, R. Falster, V. V. Voronkov, and J. Schmidt, "Lifetimes exceeding 1 ms in 1-Ω cm boron-doped Cz-silicon," *Solar*

Energy Materials and Solar Cells, vol. 131, 2014, doi: 10.1016/j.solmat.2014.06.011.

[16] N. Nampalli *et al.*, “Multiple pathways for permanent deactivation of boron-oxygen defects in p-type silicon,” *Solar Energy Materials and Solar Cells*, vol. 173, 2017, doi: 10.1016/j.solmat.2017.06.041.

[17] J. Schmidt, K. Bothe, and R. Hezel, “Structure and transformation of the metastable centre in CZ-silicon solar cells,” in *Proceedings of the 3rd World Conference on Photovoltaic Energy Conversion*, 2003.

[18] P. Hamer *et al.*, “Boron-Oxygen Defect Formation Rates and Activity at Elevated Temperatures,” in *Energy Procedia*, 2016. doi: 10.1016/j.egypro.2016.07.070.

[19] J. Schmidt and K. Bothe, “Structure and transformation of the metastable boron- and oxygen-related defect center in crystalline silicon,” *Phys Rev B Condens Matter Mater Phys*, vol. 69, no. 2, 2004, doi: 10.1103/PhysRevB.69.024107.

[20] K. Bothe, R. Sinton, and J. Schmidt, “Fundamental boron-oxygen-related carrier lifetime limit in mono- And multicrystalline silicon,” *Progress in Photovoltaics: Research and Applications*, vol. 13, no. 4, 2005, doi: 10.1002/pip.586.

[21] S. W. Glunz *et al.*, “On The Degradation of CZ-Silicon Solar Cells,” in *2nd World Conference on Photovoltaic Solar Energy Conversion, Vienna*, 1998.

[22] S. Y. Lim, F. E. Rougieux, and D. Macdonald, “Boron-oxygen defect imaging in p-type Czochralski silicon,” *Appl Phys Lett*, vol. 103, no. 9, Aug. 2013, doi: 10.1063/1.4819096.

[23] J. Adey, R. Jones, D. W. Palmer, P. R. Briddon, and S. Öberg, “Degradation of boron-doped Czochralski-grown silicon solar cells,” *Phys Rev Lett*, vol. 93, no. 5, 2004, doi: 10.1103/PhysRevLett.93.055504.

[24] S. Rein and S. W. Glunz, “Electronic properties of the metastable defect in boron-doped Czochralski silicon: Unambiguous determination by advanced lifetime spectroscopy,” *Appl Phys Lett*, vol. 82, no. 7, 2003, doi: 10.1063/1.1544431.

[25] B. J. Hallam *et al.*, “Hydrogen passivation of B-O defects in Czochralski silicon,” in *Energy Procedia*, 2013. doi: 10.1016/j.egypro.2013.07.317.

[26] C. Herring, N. M. Johnson, and C. G. Van de Walle, “Energy levels of isolated interstitial hydrogen in silicon,” *Phys Rev B Condens Matter Mater Phys*, vol. 64, no. 12, 2001, doi: 10.1103/physrevb.64.125209.

[27] D. Mathiot, “Modeling of hydrogen diffusion in *n* - and *p* -type silicon,” *Phys Rev B*, vol. 40, no. 8, pp. 5867–5870, Sep. 1989, doi: 10.1103/PhysRevB.40.5867.

[28] R. Rizk, P. De Mierry, D. Ballutaud, M. Aucouturier, and D. Mathiot, “Hydrogen diffusion and passivation processes in p- and n-type crystalline silicon,” *Phys Rev B*, vol. 44, no. 12, 1991, doi: 10.1103/PhysRevB.44.6141.

[29] D. Chen *et al.*, “Hydrogen-induced degradation: Explaining the mechanism behind light- and elevated temperature-induced degradation in n- and p-type silicon,” *Solar Energy Materials and Solar Cells*, vol. 207, 2020, doi: 10.1016/j.solmat.2019.110353.

[30] M. Vaqueiro-Contreras *et al.*, “Identification of the mechanism responsible for the boron oxygen light induced degradation in silicon photovoltaic cells,” *J Appl Phys*, vol. 125, no. 18, 2019, doi: 10.1063/1.5091759.

[31] C. Madumelu *et al.*, “Investigation of light-induced degradation in N-Type silicon heterojunction solar cells during illuminated annealing at elevated temperatures,” *Solar Energy Materials and Solar Cells*, vol. 218, 2020, doi: 10.1016/j.solmat.2020.110752.

[32] B. J. Hallam, P. G. Hamer, A. M. Ciesla née Wenham, C. E. Chan, B. Vicari Stefani, and S. Wenham, “Development of advanced hydrogenation processes for silicon solar cells via an improved understanding of the behaviour of hydrogen in silicon,” *Progress in Photovoltaics: Research and Applications*, vol. 28, no. 12, 2020, doi: 10.1002/pip.3240.

[33] R. Chen *et al.*, “23.83% efficient mono-PERC incorporating advanced hydrogenation,” *Progress in Photovoltaics: Research and Applications*, vol. 28, no. 12, 2020, doi: 10.1002/pip.3243.

[34] P. Hamer, B. Hallam, M. Abbott, C. Chan, N. Nampalli, and S. Wenham, “Investigations on accelerated processes for the boron-oxygen defect in p-type Czochralski silicon,” *Solar Energy Materials and Solar Cells*, vol. 145, 2016, doi: 10.1016/j.solmat.2015.11.013.

[35] B. Hallam *et al.*, “Rapid Processing of Boron-Oxygen Defects,” in *31st European Photovoltaic Solar Energy Conference and Exhibition*, 2015.

[36] B. J. Hallam *et al.*, “Advanced Hydrogenation of Dislocation Clusters and Boron-oxygen Defects in Silicon Solar Cells,” in *Energy Procedia*, 2015. doi: 10.1016/j.egypro.2015.07.113.

[37] Z. Y. Yeo, Z. P. Ling, J. W. Ho, Q. X. Lim, Y. H. So, and S. Wang, “Status review and future perspectives on mitigating light-induced degradation on silicon-based solar cells,” *Renewable and Sustainable Energy Reviews*, vol. 159. 2022. doi: 10.1016/j.rser.2022.112223.

[38] A. Herguth, G. Schubert, M. Kaes, and G. Hahn, “Avoiding boron-oxygen related degradation in highly boron doped Cz silicon,” in *EU-PVSEC 21st*, 2006.

[39] M. Xie, C. Ren, L. Fu, X. Qiu, X. Yu, and D. Yang, “An industrial solution to light-induced degradation of crystalline silicon solar cells,” *Frontiers in Energy*, vol. 11, no. 1, 2017, doi: 10.1007/s11708-016-0430-x.

[40] A. Herguth, “Quantification of Iron in Boron-Doped Silicon Solar Cells from Open Circuit Voltage Measurements,” *IEEE J Photovolt*, vol. 12, no. 4, 2022, doi: 10.1109/JPHOTOV.2022.3168134.

[41] J. Schmidt, “Effect of dissociation of iron-boron Pairs in crystalline silicon on solar cell properties,” *Progress in Photovoltaics: Research and Applications*, vol. 13, no. 4, 2005, doi: 10.1002/pip.594.

[42] G. Zoth and W. Bergholz, “A fast, preparation-free method to detect iron in silicon,” *J Appl Phys*, vol. 67, no. 11, 1990, doi: 10.1063/1.345063.

[43] L. C. Kimerling and J. L. Benton, “Electronically controlled reactions of interstitial iron in silicon,” *Physica B+C*, vol. 116, no. 1–3, 1983, doi: 10.1016/0378-4363(83)90263-2.

[44] D. Macdonald, T. Roth, P. N. K. Deenapanray, K. Bothe, P. Pohl, and J. Schmidt, “Formation rates of iron-acceptor pairs in crystalline silicon,” *J Appl Phys*, vol. 98, no. 8, 2005, doi: 10.1063/1.2102071.

[45] D. H. Macdonald, L. J. Geerligs, and A. Azzizi, “Iron detection in crystalline silicon by carrier lifetime measurements for arbitrary injection and doping,” *J Appl Phys*, vol. 95, no. 3, 2004, doi: 10.1063/1.1637136.

[46] D. MacDonald, J. Tan, and T. Trupke, “Imaging interstitial iron concentrations in boron-doped crystalline silicon using photoluminescence,” *J Appl Phys*, vol. 103, no. 7, 2008, doi: 10.1063/1.2903895.

[47] M. Kouketsu and S. Isomae, “Hydrogen passivation of iron-related hole traps in silicon,” *J Appl Phys*, vol. 80, no. 3, 1996, doi: 10.1063/1.363018.

[48] A. Liu, C. Sun, and D. MacDonald, “Hydrogen passivation of interstitial iron in boron-doped multicrystalline silicon during annealing,” *J Appl Phys*, vol. 116, no. 19, 2014, doi: 10.1063/1.4901831.

[49] R. Singh, S. J. Fonash, and A. Rohatgi, “Interaction of low-energy implanted atomic H with slow and fast diffusing metallic impurities in Si,” *Appl Phys Lett*, vol. 49, no. 13, 1986, doi: 10.1063/1.97551.

[50] P. Karzel, A. Frey, S. Fritz, and G. Hahn, “Influence of hydrogen on interstitial iron concentration in multicrystalline silicon during annealing steps,” *J Appl Phys*, vol. 113, no. 11, 2013, doi: 10.1063/1.4794852.

[51] K. Ramspeck, “Light induced degradation of rear passivated mc-Si solar cells,” *27th European Photovoltaic Solar Energy Conference and Exhibition LIGHT*, vol. 91, no. 5, 2012.

[52] F. Kersten *et al.*, “A new mc-Si degradation effect called LeTID,” in *2015 IEEE 42nd Photovoltaic Specialist Conference, PVSC 2015*, 2015. doi: 10.1109/PVSC.2015.7355684.

[53] H. C. Sio, D. Kang, X. Zhang, J. Yang, J. Jin, and D. MacDonald, “The Role of Dark Annealing in Light and Elevated Temperature Induced Degradation in p-Type Mono-Like Silicon,” *IEEE J Photovolt*, vol. 10, no. 4, 2020, doi: 10.1109/JPHOTOV.2020.2993653.

[54] D. Chen *et al.*, “Hydrogen induced degradation: A possible mechanism for light- and elevated temperature- induced degradation in n-type silicon,” *Solar Energy Materials and Solar Cells*, vol. 185, 2018, doi: 10.1016/j.solmat.2018.05.034.

[55] D. Chen *et al.*, “Evidence of an identical firing-activated carrier-induced defect in monocrystalline and multicrystalline silicon,” *Solar Energy Materials and Solar Cells*, vol. 172, 2017, doi: 10.1016/j.solmat.2017.08.003.

[56] T. Niewelt, M. Selinger, N. E. Grant, W. Kwapil, J. D. Murphy, and M. C. Schubert, “Light-induced activation and deactivation of bulk defects in boron-doped float-zone silicon,” *J Appl Phys*, vol. 121, no. 18, May 2017, doi: 10.1063/1.4983024.

[57] F. Kersten, J. Heitmann, and J. W. Müller, “Influence of Al2O3 and SiNx Passivation Layers on LeTID,” in *Energy Procedia*, 2016. doi: 10.1016/j.egypro.2016.07.079.

[58] C. Vargas *et al.*, “Carrier-Induced Degradation in Multicrystalline Silicon: Dependence on the Silicon Nitride Passivation Layer and Hydrogen Released during Firing,” *IEEE J Photovolt*, vol. 8, no. 2, 2018, doi: 10.1109/JPHOTOV.2017.2783851.

[59] J. Simon *et al.*, “Correlation study between LeTID defect density, hydrogen and firing profile in Ga-doped crystalline silicon,” *Solar Energy Materials and Solar Cells*, vol. 260, 2023, doi: 10.1016/j.solmat.2023.112456.

[60] D. Bredemeier, D. Walter, S. Herlufsen, and J. Schmidt, “Understanding the Light-induced Lifetime Degradation and Regeneration in Multicrystalline Silicon,” in *Energy Procedia*, 2016. doi: 10.1016/j.egypro.2016.07.060.

[61] J. F. Lelièvre, E. Fourmond, A. Kaminski, O. Palais, D. Ballutaud, and M. Lemiti, “Study of the composition of hydrogenated silicon nitride SiNx:H for efficient surface and bulk passivation of silicon,” *Solar Energy Materials and Solar Cells*, vol. 93, no. 8, 2009, doi: 10.1016/j.solmat.2009.01.023.

[62] T. Niewelt, F. Schindler, W. Kwapil, R. Eberle, J. Schön, and M. C. Schubert, “Understanding the light-induced degradation at elevated temperatures: Similarities between multicrystalline and floatzone p-type silicon,” *Progress in Photovoltaics: Research and Applications*, vol. 26, no. 8, 2018, doi: 10.1002/pip.2954.

[63] C. Chan *et al.*, “Modulation of Carrier-Induced Defect Kinetics in Multi-Crystalline Silicon PERC Cells Through Dark Annealing,” *Solar RRL*, vol. 1, no. 2, 2017, doi: 10.1002/solr.201600028.

[64] A. Van Wieringen and N. Warmoltz, “On the permeation of hydrogen and helium in single crystal silicon and germanium at elevated temperatures,” *Physica*, vol. 22, no. 6–12, 1956, doi: 10.1016/S0031-8914(56)90039-8.

[65] S. J. Pearton, J. W. Corbett, and J. T. Borenstein, “Hydrogen diffusion in crystalline semiconductors,” *Physica B: Physics of Condensed Matter*, vol. 170, no. 1–4, pp. 85–97, 1991, doi: 10.1016/0921-4526(91)90109-R.

[66] J. Weber, “Hydrogen in semiconductors: From basic physics to technology,” in *Physica Status Solidi (C) Current Topics in Solid State Physics*, 2008. doi: 10.1002/pssc.200776819.

[67] P. Hamer, B. Hallam, R. S. Bonilla, P. P. Altermatt, P. Wilshaw, and S. Wenham, “Modelling of hydrogen transport in silicon solar cell structures under equilibrium conditions,” *J Appl Phys*, vol. 123, no. 4, 2018, doi: 10.1063/1.5016854.

[68] C. G. Van De Walle and J. Neugebauer, “Hydrogen in semiconductors,” *Annu Rev Mater Res*, vol. 36, pp. 179–198, 2006, doi: 10.1146/annurev.matsci.36.010705.155428.

[69] P. Hamer, H. Li, C. Chan, C. Sen, R. S. Bonilla, and P. Wilshaw, “The Behavior and Transport of Hydrogen in Silicon Solar Cells Observed through Changes in Contact Resistance,” in *2018 IEEE 7th World Conference on Photovoltaic Energy Conversion, WCPEC 2018 - A Joint Conference of 45th IEEE PVSC, 28th PVSEC and 34th EU PVSEC*, 2018. doi: 10.1109/PVSC.2018.8547880.

[70] G. Bektaş *et al.*, “A comparative study on alternative industrial manufacturing routes for bifacial n-PERT silicon solar cells,” *Progress in Photovoltaics: Research and Applications*, vol. 31, no. 10, 2023, doi: 10.1002/pip.3706.

[71] S. Jafari, J. Hirsch, D. Lausch, M. John, N. Bernhard, and S. Meyer, “Composition limited hydrogen effusion rate of a-SiNx:H passivation stack,” in *AIP Conference Proceedings*, 2019. doi: 10.1063/1.5123853.

[72] G. Krugel, W. Wolke, J. Geilker, S. Rein, and R. Preu, “Impact of hydrogen concentration on the regeneration of light induced degradation,” in *Energy Procedia*, 2011. doi: 10.1016/j.egypro.2011.06.100.

[73] J. Simon *et al.*, “Correlation study between LeTID defect density, hydrogen and firing profile in Ga-doped crystalline silicon,” *Solar Energy Materials and Solar Cells*, vol. 260, Sep. 2023, doi: 10.1016/j.solmat.2023.112456.

[74] D. C. Walter, D. Bredemeier, R. Falster, V. V. Voronkov, and J. Schmidt, “Easy-to-apply methodology to measure the hydrogen concentration in boron-doped crystalline silicon,” *Solar Energy Materials and Solar Cells*, vol. 200, 2019, doi: 10.1016/j.solmat.2019.109970.

[75] D. Bredemeier, D. Walter, R. Heller, and J. Schmidt, “Impact of Silicon Nitride Film Properties on Hydrogen in-Diffusion Into Crystalline Silicon,” *36th European Photovoltaic Solar Energy Conference and Exhibition*, no. November, 2019.

[76] S. J. Choi, G. J. Yu, G. H. Kang, J. C. Lee, D. Kim, and H. E. Song, “The electrical properties and hydrogen passivation effect in mono crystalline silicon solar cell with various pre-deposition times in doping process,” *Renew Energy*, vol. 54, 2013, doi: 10.1016/j.renene.2012.08.052.

[77] B. Sopori, Y. Zhang, and N. M. Ravindra, “Silicon device processing in H-ambients: H-diffusion mechanisms and influence on electronic properties,” *J Electron Mater*, vol. 30, no. 12, 2001, doi: 10.1007/s11664-001-0181-1.

[78] A. Herguth and C. Winter, “Methodology and Error Analysis of Direct Resistance Measurements Used for the Quantification of Boron-Hydrogen Pairs in Crystalline Silicon,” *IEEE J Photovolt*, vol. 11, no. 4, 2021, doi: 10.1109/JPHOTOV.2021.3074463.

[79] V. V. Voronkov and R. Falster, “Formation, dissociation, and diffusion of various hydrogen dimers in silicon,” *Phys Status Solidi B Basic Res*, vol. 254, no. 6, 2017, doi: 10.1002/pssb.201600779.

[80] S. Ding *et al.*, “Comparison of LID and Electrical Injection Regeneration of PERC and Al-BSF Solar Cells from a Cz-Si Ingot,” *Energies (Basel)*, vol. 15, no. 20, 2022, doi: 10.3390/en15207764.

[81] H. H. Canar, G. Bektaş, and R. Turan, “On the passivation performance of SiNx, SiOxNy and their stack on c-Si wafers for solar cell applications: Correlation with optical, chemical and interface properties,” *Solar Energy Materials and Solar Cells*, vol. 256, 2023, doi: 10.1016/j.solmat.2023.112356.

[82] R. A. Sinton, A. Cuevas, and M. Stuckings, “Quasi-steady-state photoconductance, a new method for solar cell material and device characterization,” in *Conference Record of the IEEE Photovoltaic Specialists Conference*, 1996. doi: 10.1109/pvsc.1996.564042.

[83] I. Tarasov, S. Ostapenko, K. Nakayashiki, and A. Rohatgi, “Defect passivation in multicrystalline silicon for solar cells,” in *Applied Physics Letters*, 2004. doi: 10.1063/1.1815380.

[84] S. Ostapenko, I. Tarasov, J. P. Kalejs, C. Haessler, and E. U. Reisner, “Defect monitoring using scanning photoluminescence spectroscopy in multicrystalline silicon wafers,” *Semicond Sci Technol*, vol. 15, no. 8, 2000, doi: 10.1088/0268-1242/15/8/310.

[85] G. Bektas *et al.*, “Optimization of front and rear surface dielectric passivation layers for ion implanted PERC solar cells,” in *AIP Conference Proceedings*, 2023. doi: 10.1063/5.0140410.

[86] F. Fertig *et al.*, “Excessive light-induced degradation in boron-doped Cz silicon PERC triggered by dark annealing,” *Solar Energy Materials and Solar Cells*, vol. 200, 2019, doi: 10.1016/j.solmat.2019.109968.

[87] W. M. Bullis and H. R. Huff, “Interpretation of Carrier Recombination Lifetime and Diffusion Length Measurements in Silicon,” *J Electrochem Soc*, vol. 143, no. 4, 1996, doi: 10.1149/1.1836650.

[88] S. Rein and S. W. Glunz, “Electronic properties of interstitial iron and iron-boron pairs determined by means of advanced lifetime spectroscopy,” *J Appl Phys*, vol. 98, no. 11, 2005, doi: 10.1063/1.2106017.

[89] M. Yli-Koski *et al.*, “Recombination activity of iron in boron doped silicon,” in *Physica Scripta T*, 2002. doi: 10.1238/physica.topical.101a00086.